LINEAR ANALYSIS OF SURFACE TEMPERATURE DYNAMICS AND CLIMATE SENSITIVITY

A Dissertation

by

WEI WU

Submitted to the Office of Graduate Studies of
Texas A&M University
in partial fulfillment of the requirements for the degree of

DOCTOR OF PHILOSOPHY

December 2005

Major Subject: Oceanography

LINEAR ANALYSIS OF SURFACE TEMPERATURE DYNAMICS AND CLIMATE SENSITIVITY

A Dissertation

by

WEI WU

Submitted to the Office of Graduate Studies of
Texas A&M University
in partial fulfillment of the requirements for the degree of

DOCTOR OF PHILOSOPHY

Approved by:

Co-Chairs of Committee,	Gerald R. North
	Ping Chang
Committee Members,	Achim Stoessel
	Kenneth P. Bowman
	Robert Scott
Head of Department,	Wilford D. Gardner

December 2005

Major Subject: Oceanography

ABSTRACT

Linear Analysis of Surface Temperature Dynamics and Climate Sensitivity.

(December 2005)

Wei Wu, B.S., Ocean University of China;

M.S., Ocean University of China

Co-Chairs of Advisory Committee: Dr. Gerald R. North
Dr. Ping Chang

Spectral properties of global surface temperature and uncertainties of global climate sensitivity are explored in this work through the medium of Energy Balance Climate Models (EBCMs) and observational surface temperature data.

In part I, a complete series of 2D time-dependent non-orthogonal eigenmodes of global surface temperature are analytically derived and their geographic patterns are presented. The amplitudes of these modes have temporal characteristics and present exponentially decaying patterns. Theoretically, if the energy balance model is forced by white noise forcing in time, the autocorrelation functions of the mode amplitudes should present the same exponentially decaying patterns. When observed surface temperature data are projected onto these theoretical modes, the autocorrelation time scales of the mode amplitudes exhibit similar exponential decaying patterns. These modes are believed to be useful for surface temperature studies and model intercomparison.

In part II, an objective means of deriving the probability density function (PDF) of global climate sensitivity is investigated. The method constrains the PDF by its fit to the present climate in terms of surface temperature. We found that a wide range of

parameter combinations, which corresponds to a broad range of the sensitivity, shows equally good fits to the present climate. It means that the uncertainties in global climate sensitivity are very difficult to eliminate if climate models are tuned to fit observations of surface temperature alone. The origin of the skewness of the PDF is found in very simple terms.

DEDICATION

To my loving family

ACKNOWLEDGMENTS

I am heartfeltly grateful to my advisor Prof. Gerald R. North for his great guidance, persistent encouragement and strong support during this work. I am indebted to my co-advisor Prof. Ping Chang for his generous financial support and very helpful advice on observational data and numerical techniques. My gratitude also goes to my committee members Prof. Achim Stoessel, Prof. Kenneth P. Bowman and Dr. Robert Scott for their very nice advice and help. I appreciate all the wonderful lectures I had here by Prof. Gerald R. North, Prof. Ping Chang, Prof. Robert Stewart, Prof. Benjamin Giese, Prof. Robert Hetland, Prof. Steven Dimarco, Dr. R. Saravanan and Porf. Niall Slowey. Thanks to Department Head Prof. Wilford D. Gardner, Prof. Robert Stewart, Dr. Link Ji, Prof. Ayal Anis, Department Staff members and all others whoever provided me valuable discussions and kind help. Special thanks to Neil Smith and Mark McCann for strong support on computer work. Of course, I appreciate all my friends for friendship and encouragement during the 4 years.

TABLE OF CONTENTS

Page

LIST OF FIGURES

FIGURE Page

LIST OF TABLES

CHAPTER I

INTRODUCTION

The Earth system absorbs energy through solar radiation non-uniformly, driving winds and currents in the ocean-atmosphere system, these in turn leading to a large number of interactive processes such as moisture, heat and momentum exchange (Gill 1982). These processes ultimately control the distribution of heating at the earth's surface and make the surface temperature vary with time and space. Energy conservation constrains the earth's surface temperature to be determined by a balance of the rate of incoming solar energy absorbed by the Earth and the rate of outgoing energy by infrared radiation and other non-radiative processes. Due to the nonlinearity and coupling of the system, to determine how the atmosphere and ocean respond to radiation from the sun is not easy. Climate sensitivity is indicated by the steady-state change in globally and annually averaged temperature for a doubling of the concentration of CO_2 in the atmosphere. It is a key determinant of climate change and its large uncertainties remain in recent studies. In this work we employ a statistical-dynamical approach to explore surface temperature dynamics and climate sensitivity through the medium of Energy Balance Climate Models (EBCMs) in an effort to bring a better understanding for the

---

This dissertation follows the style and format of *Journal of Climate*.

spectral behaviors of the Earth surface temperature and for the origin of the uncertainties in global climate sensitivity.

EBCMs are simple climate models whose solutions yield the surface temperature field and its variability as reviewed by North et al. (1981). The major advantage of these models is that they have only a few adjustable parameters and therefore solutions can be easily extracted by either analytical or reliable numerical procedures. The disadvantage of these models is that they do not have an advection term and some non-radiative heat flux terms such as latent and sensible heat fluxes are highly simplified. The fundamental principle of the climate models is the conservation of energy for each infinitesimal horizontal cross-section of Earth-Atmosphere column.

EBCMs account for the energy fluxes into and out of the Earth-Atmosphere column. All the fluxes are parameterized in terms of the surface temperature field (North et al. 1981). Horizontal heat transports are parameterized by simple diffusive mechanisms and the infrared radiation to space by an empirical linear form in surface temperature. EBCMs have proven to be useful models for examing idealized climate systems and for exploring questions that large models could not handle (North 1975 (a), North 1975 (b), North and Coakley 1978, North and Coakley 1979, Cahalan and North 1979, Salmun et al. 1980, North and Cahalan 1981, Short et al. 1984, North 1984 (a), Hyde et al. 1989, North 1990, Leung and North 1990, Leung and North 1991, Graves et al. 1993, Kim et al. 1996). They have been successful in modeling climate and climate change related to the surface temperature field and have been making contributions to climate studies for three decades (James and North 1982, North et al. 1983, North 1984

(b), North and Crowley 1985, Crowley et al. 1986, Crowley and North 1988, Mengel et al. 1988, Lin and North 1990, Hyde et al 1990, Crowley and North 1990, Newton et al. 1990, Short et al. 1991, Kim and North 1991, Leung and North 1991, Crowley and North 1991, Kim and North 1992, Kim et al. 1992, Huang and Bowman 1992, Kim and North 1993, Lee and North 1995, Kim and North 1995, North and Kim 1995, North et al. 1995, Stevens and North 1996, North and Stevens 1998, Goody et al. 1998, Shen and North 1999, North and Wu 2001). The phenomenological parameters such as diffusion or radiative damping coefficients in EBCMs cannot be derived directly but rather have to be fitted to real data (North et al. 1981). A few such adjustable parameters are required to obtain good fits to the geographical distribution of such quantities as the mean seasonal cycle and the distribution of variance over a wide range of frequency bands. The time scale separation of the eddies that transport most of the heat, and the radiative relaxation time of a column of air or the mixed layer of the ocean lead to the success of the models in reproducing the observed fields.

This dissertation is organized as follows. Chapter II introduces the derivation, properties and applications of a complete set of time independent non-orthogonal thermal decay modes (TDMs) of global surface temperature, which can be used as a basis set for surface temperature fields. Chapter III introduces an objective means of deriving the probability density function (PDF) of climate sensitivity constrained by the present climate and explains the possible causes of the uncertainty in global climate sensitivity. A summary follows in Chapter IV that gives conclusions of this work and some discussions for further studies.

CHAPTER II

LINEAR ANALYSIS OF SURFACE TEMPERATURE DYNAMICS

2.1. Introduction

The earliest studies of estimating the Earth's surface temperature can be traced back to the 19th century, with rather crude calculations for the energy balance of the whole planet such as Arrhenius (1896), reviewed by Hunt et al. (1986). The pioneer Dines (1917) developed the first explicit model including infrared radiation upward and downward from the atmosphere itself, and energy moved up from the Earth's surface into the atmosphere in the form of heat carried by moisture (Hunt et al. 1986). He assumed that no appreciable temperature change happens in time and so his Earth-Atmosphere system should balance radiative equilibrium. He assumed a solar constant is of 1388 W m^{-2} and albedo of 0.50. His mathematical approach suggested an effective temperature of the Earth to be 242 K and the temperature decreases with altitude, to approximately 210 K mean temperature at 20km in altitude (Hunt et al. 1986). Subsequently, simple or advanced energy balance models (North et al. 1981), radiative-convective models (reviewed by Ramanathan and Coakley 1978) and general circulation models (McGuffie and Henderson-Sellers 1997, Washington and Parkinson 2005) and stochastic models (reviewed by Saltzman 1978) helped climate scientists feel out the basic physical principles of climate in the Earth-Atmosphere system and reveal the properties of the climate variability through the balance of energy budget in the system (e.g., Schneider

and Dickinson 1974, North and Coakley 1979, North et al. 1983, Hansen and Lebedeff 1987, Schlesinger 1989, Chang et al. 1997, Andronova and Schlesinger 2001, Sun and Hansen 2003, Murphy et al. 2004, Stainforth et al. 2005, Meehl et al. 2005, Hansen et al. 2005). However, we have relatively little insight about the surface temperature's spatial spectral behavior though we have been successful in obtaining practical solutions numerically. Some basis sets, such as Empirical Orthogonal Functions, have been used in studying global surface temperature and proven to be useful (e.g., North and Cahalan 1981, North et al. 1983, North 1984(a), Hyde et al. 1989, Kim and North 1993, Kim et al. 1996, North and Wu 2001). But because of the highly irregular land-sea distribution, these basis functions are not actually dynamical modes. In this chapter, we will develop a complete set of non-orthogonal eigenfunctions from a 2-D Energy Balance Climate Model (EBCM) which have (linear) dynamical significance and exhibit very distinct geometrical and family behaviors.

2.2. Deriving Thermal Decay Modes

The EBCM we used was introduced by North et al. (1983), hereafter, NMS83. The Earth-Atmosphere system is taken to be the whole column from the top of atmosphere to the ground over land or to the depth of the mixed layer over ocean. The temperature at any given point is characterized as the mean temperature of the whole column at the point. It is assumed that this column average can be characterized by its surface value. It includes the land-sea geography through a heat capacity function $C(\vec{r})$, which is large over ocean (estimated from the mixed layer depth) and about two orders

of magnitude smaller over land (characteristic of atmosphere-land column). Heat transport is controlled by latitude-dependent horizontal diffusion only.

This model can be written as

$$C(\hat{r})\frac{\partial T(\hat{r},t)}{\partial t} - \nabla \cdot (D(\hat{r})\nabla T(\hat{r},t)) + A + BT(\hat{r},t) = F(\hat{r},t) \tag{2.1}$$

where $T(\hat{r},t)$ is the surface temperature at point $\hat{r}$ and time t, $C(\hat{r})$ is the heat capacity, $D(\hat{r})$ is a thermal conductivity coefficient which might depend upon position on the sphere, $A+BT$ is the rate of outgoing infrared radiation to space with A and B empirical coefficients derived from satellite measurements (Short et al. 1984, Graves et al. 1993), and $F(\hat{r},t)$ is a forcing which could include the solar radiation energy absorbed by the Earth-Atmosphere system and a noise forcing representing weather fluctuations. Here the cloud forcing from the infrared radiation is assumed to exactly cancel the cloud forcing due to the solar radiation.

The equation of the temperature departure (remove the annual-mean part) formed by (2.1) is

$$C(\hat{r})\frac{\partial \tilde{T}(\hat{r},t)}{\partial t} - \nabla \cdot (D(\hat{r})\nabla \tilde{T}(\hat{r},t)) + B\tilde{T}(\hat{r},t) = \tilde{F}(\hat{r},t) \tag{2.2}$$

$\tilde{F}(\hat{r},t)$ represents periodic and/or noise forcing. If $\tilde{F}(\hat{r},t)$ is assumed to be zero, we can analytically solve the linear equation (2.2) by setting $\tilde{T}(\hat{r},t) = \psi(\hat{r})e^{-\lambda t}$. This leads to a generalized Sturm-Liouville eigenvalue problem as follows

$$(-\nabla D(\hat{r}) \cdot \nabla + B)\psi(\hat{r}) = \lambda C(\hat{r})\psi(\hat{r}) \tag{2.3}$$

The LHS operator $-\nabla D(\hat{r})\cdot\nabla + B$ is Hermitian (Horn and Johnson 1985). Boundary conditions are no heat flux entering the poles. The result is a complete basis set of eigenfunctions $\psi_n(\hat{r})$ (referred to here as the Thermal Decay Modes) corresponding to eigenvalues λ_n (n = 1, 2, 3,……). These eigenvalues and eigenfunctions are real (Horn and Johnson 1985). Here $C(\hat{r})/B$ has dimension time and represents the characteristic time for relaxation if the entire planet had the uniform heat capacity $C(\hat{r})$ at each point $\hat{r}$, and $D(\hat{r})/B$ represents the square of a local length scale (North 1984 (b)).

We can then easily derive the orthogonality properties of $\psi_n(\hat{r})$ (n = 1, 2, 3,……) from (2.3) by using the Hermitian property of $-\nabla D(\hat{r})\cdot\nabla + B$ and $C(\hat{r})$ (detailed derivation in Appendix A). The $\psi_n(\hat{r})$ can be normalized such that

$$(\psi_{m,} C\psi_n) = \delta_{m,n} \tag{2.4}$$

Here the standard inner product notation is adopted

$$(\psi,\phi) = \int \psi^*(\hat{r})\phi(\hat{r})d\hat{r} \tag{2.5}$$

where the superscript asterisk indicates complex conjugation, and $d\hat{r}$ indicates integration with respect to solid angle over the entire sphere. Note that if we set $C_{ocean} \to \infty$, the only temperature response occurs over land for time dependent forcing and the land eigenfunctions become orthogonal (without the need for the weight function $C(\hat{r})$). At high frequencies (f >>1/year), this can be a good approximation.

The temperature departure $\tilde{T}(\hat{r},t)$ can be expanded into the $\psi_n(\hat{r})$ as

$$\tilde{T}(\hat{r},t) = \sum_n a_n(t)\psi_n(\hat{r}) \tag{2.6}$$

with

$$a_n(t) = (\psi_n, C\tilde{T}) \tag{2.7}$$

By plugging (2.6) back into (2.2), we can get the Fluctuation-Dissipation Equation of the Earth-Atmosphere system as

$$\dot{a}_n + \lambda_n a_n = (\psi_n, \tilde{F}), \quad n = 1, 2, 3, ... \tag{2.8}$$

Discussions on Fluctuation-Dissipation in climate and climate modeling can be found in Leith (1975), Hasselmann (1976), Bell (1980), North et al. (1993) and Von Storch (2004).

If we set $\tilde{F}(\hat{r}, t)$ to zero, each mode amplitude $a_n(t)$ will decay exponentially to zero with time constant $\tau_n = 1/\lambda_n$. It is shown in the following that if the forcing $\tilde{F}(\hat{r}, t)$ consists of white spatial noise, the $a_n(t)$ may be correlated from one mode to another and therefore they are not statistically independent even though the forcing is uncorrelated from point to point. Assume that

$$\tilde{F}(\hat{r}, t) = F_\omega(\hat{r}) e^{-i\omega t} \tag{2.9}$$

and

$$a_n(t) = a_{\omega,n} e^{-i\omega t} \tag{2.10}$$

By inserting (2.9) and (2.10) into (2.8), we get

$$a_{\omega,n} = \frac{(\psi_n, F_\omega)}{\lambda_n - i\omega} \tag{2.11}$$

So,

$$< a^*_{\omega,n} a_{\omega',m} >= \frac{< (F_\omega, \psi_n)(\psi_m, F_{\omega'}) >}{(\lambda_n + i\omega)(\lambda_m - i\omega')} = \frac{\iint \psi^*_n(\hat{r}) < F^*_\omega(\hat{r}) F_{\omega'}(\hat{r}') > \psi_m(\hat{r}') d\hat{r} d\hat{r}'}{(\lambda_n + i\omega)(\lambda_m - i\omega')} \delta(\omega - \omega') \tag{2.12}$$

where <> denotes ensemble average.

If $F_\omega(\hat{r})$ is set to be white spatial noise, i.e.,

$$< F^*_\omega(\hat{r}) F_{\omega'}(\hat{r}') >= \delta(\hat{r} - \hat{r}') \tag{2.13}$$

then

$$< a^*_{\omega,n} a_{\omega',m} >= \frac{\iint \psi^*_n(\hat{r}) \psi_m(\hat{r}') \delta(\hat{r} - \hat{r}') d\hat{r} d\hat{r}'}{(\lambda_n + i\omega)(\lambda_m - i\omega')} \delta(\omega - \omega') = \frac{(\psi_n, \psi_m)}{(\lambda_n + i\omega)(\lambda_m - i\omega)} \neq 0 \tag{2.14}$$

If the $\tilde{F}(\hat{r}, t)$ is white in time, the mode amplitudes will have exponentially decaying autocorrelation functions (derivation see Appendix C)

$$\frac{< a_n(t) a_n(t + \tau_n) >}{< a_n(t) a_n(t) >} = e^{-\lambda_n \tau_n} \tag{2.15}$$

The spectrum of relaxation time scale for each mode is

$$\tau_n = 1/\lambda_n \tag{2.16}$$

2.3. Computing Thermal Decay Modes

We construct a 64 (longitude) × 33 (sin(latitude)) grid of points on the sphere to calculate our Thermal Decay Modes (TDMs). The grids are equally spaced on this rectangular map in longitude versus sin of latitude. The modes' patterns and their decay times can be modeled through (2.3) (detailed numerical procedures in Appendix B). The modes are very interesting due to their family-style

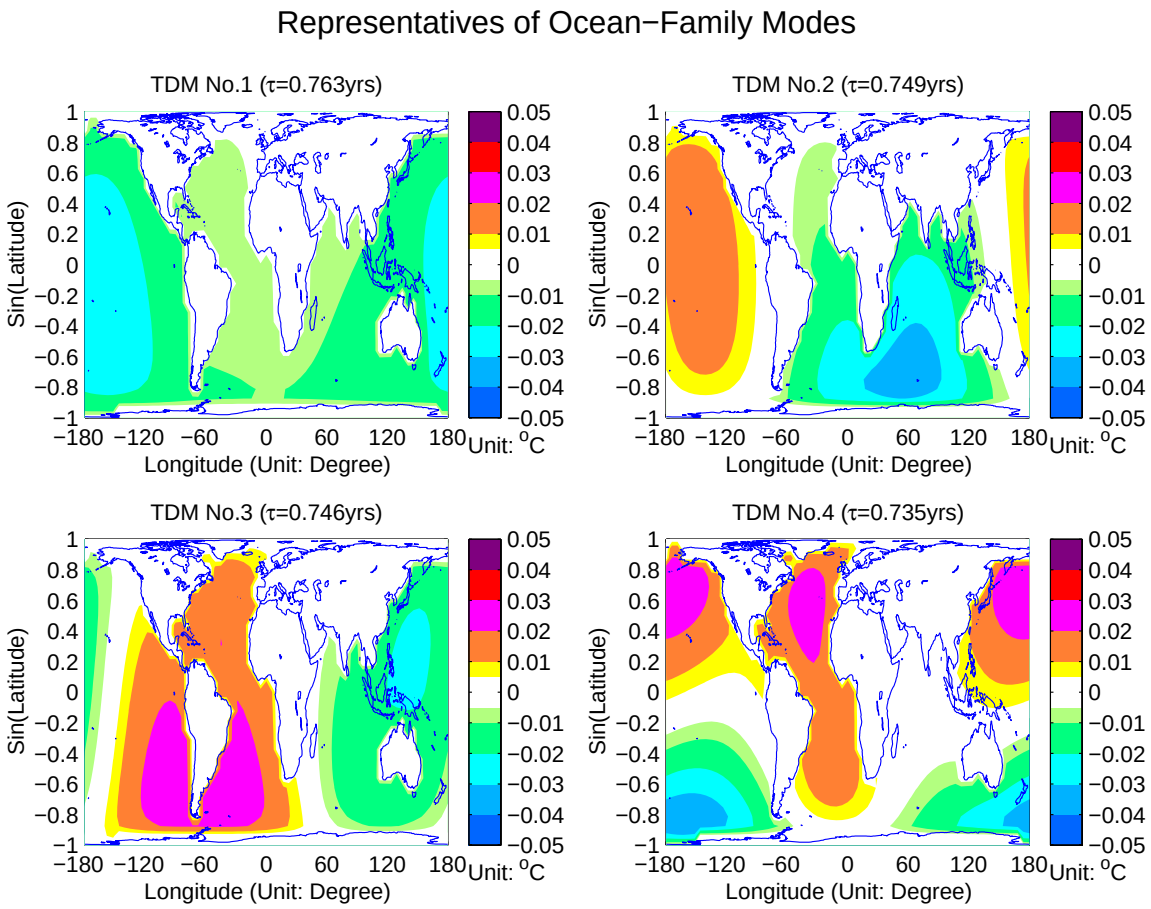

Fig. 1. Ocean-family modes. These four thermal decay modes with longest decay time scales (listed above each panel) as large scale oceanic modes.

geographic patterns. The essential difference between these modes and the EOF modes (Kim et al. 1993) is that they are spatial physical modes and their shapes do not depend on frequency as the statistical modes do. Also they are not strictly orthogonal like EOFs ($C(\hat{r})$ is the required weight function). The TDMs are sorted by their decay times, the

longest decay time having the lowest index. Figure 1 shows the first four TDMs. After $n = 1282$, the modes are associated with the land masses. Figure 2 presents 1282th,

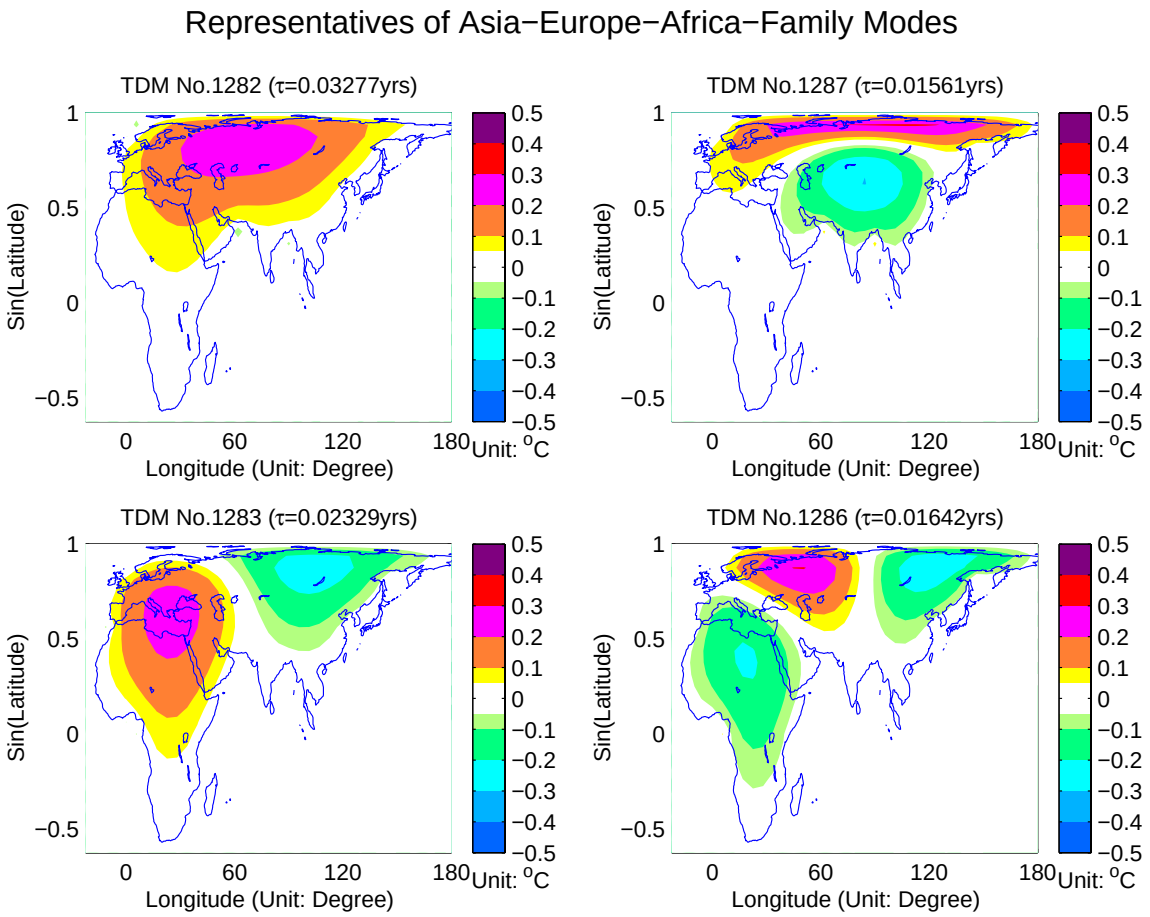

Fig. 2. Eurasian-African-family modes. These four thermal decay modes are examples of land modes over Eurasian and African continents.

1283th, 1286th and 1287th modes as examples. This family of modes is associated with the land masses of Asia-Europe-Africa with shorter and shorter decay times. The

amplitude over the rest of the world can be ignored. It is actually zero in the limit $C_{ocean} \to \infty$. Figures 3 and 4 show similar sequences for North America and Australia. The other land masses such as South America and Antarctica have similar families of

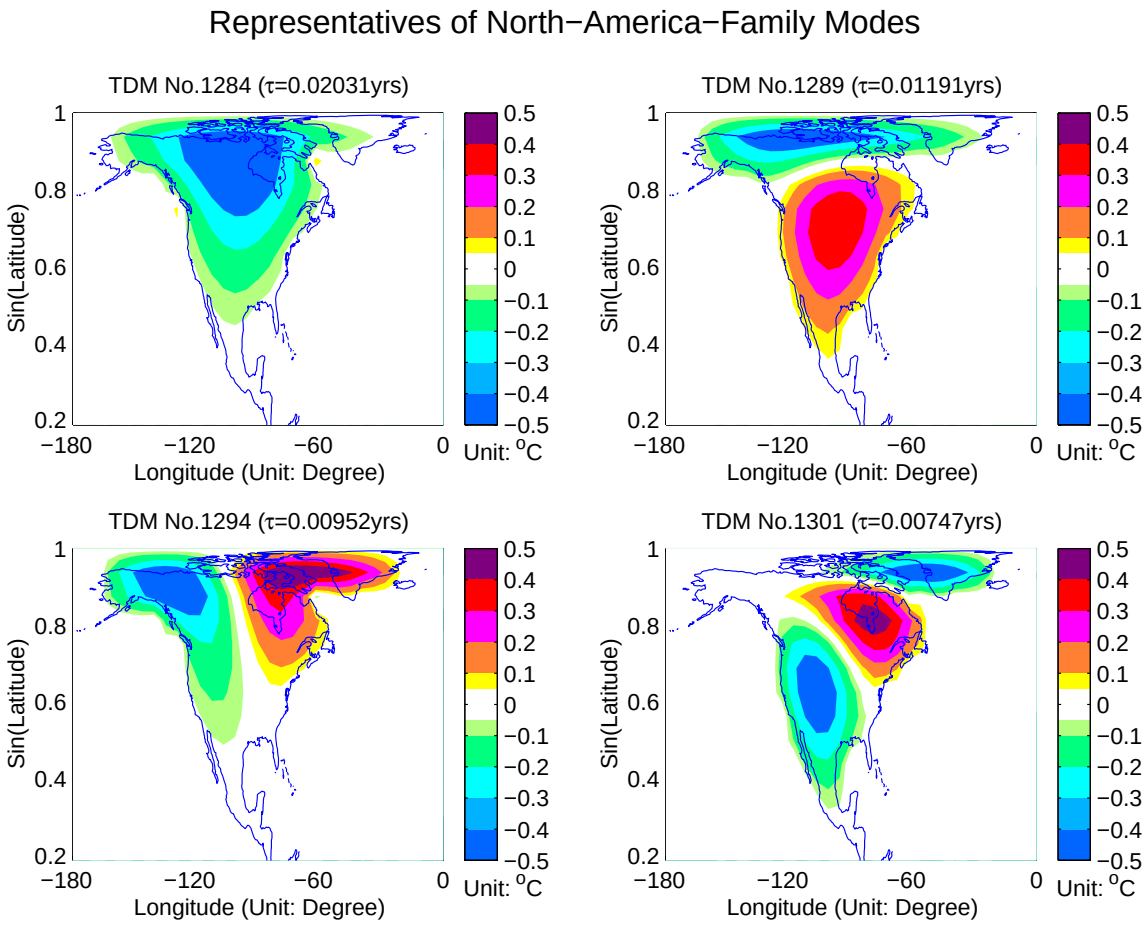

Fig. 3. North-American-family modes. These four thermal decay modes are examples of land modes over North America.

modes with negligible amplitude outside their coastlines. It is worth mentioning that the TDM shapes are hardly changed when we choose different sets of parameters such as those taken from NMS83 versus from Hyde et al. 1990. The various choices of parameters $D(\hat{r})$ and B also have almost no effect on the TDM patterns. However, the changes of the eigenvalues are significant as these parameters are varied. Therefore, the

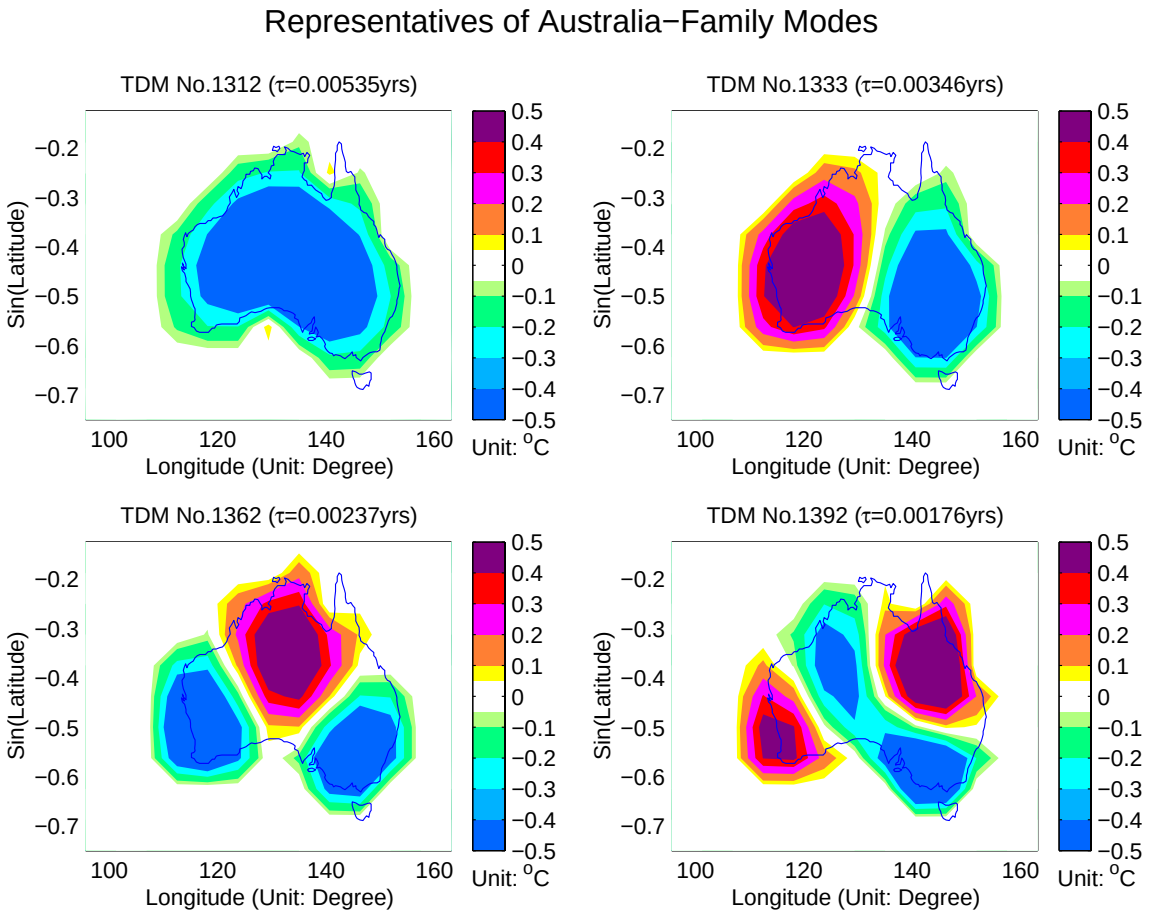

Fig. 4. Australian-family modes. These four thermal decay modes are examples of land modes over Australia.

TDM patterns are fairly robust with respect to a wide range of parameter choices, but their decay-time scales depend considerably on the model parameter settings.

2.4. Responses to Mean and Periodic Forcings

Suppose that the Earth-Atmosphere system (2.2) is driven by periodic forcing represented as the real part of $\tilde{F}(\hat{r},t)$

$$\tilde{F}(\hat{r},t) = F_{\omega}(\hat{r})e^{-i\omega(t-\alpha)} \overset{set(\alpha=0)}{=} F_{\omega}(\hat{r})e^{-i\omega t} \tag{2.17}$$

The temperature response to this forcing should be

$$\tilde{T}(\hat{r},t) = \sum_{n} a_n(t)\psi_n(\hat{r}) \tag{2.18}$$

with

$$a_n(t) = a_{\omega,n}e^{-i\omega t} \tag{2.19}$$

By substituting (2.17) and (2.19) into the Fluctuation-Dissipation Equation (2.8), we have (2.11), i.e.,

$$a_{\omega,n} = \frac{(\psi_n, F_{\omega})}{\lambda_n - i\omega} \tag{2.11}$$

By plugging (2.11) into (2.19) and then putting the $a_n(t)$ expression back into (2.18), we get

$$\tilde{T}(\hat{r},t) = \left|A(\hat{r})\right|e^{i\alpha(\hat{r})}e^{-i\omega t} \tag{2.20}$$

with

$$\left|A(\hat{r})\right| = (a^2 + b^2)^{1/2}$$

$$\alpha(\hat{r}) = arctg(b/a)$$

$$a = \sum_{n=1}^{m} \frac{(\psi_n, F_\omega)}{\lambda_n^2 + \omega^2} \lambda_n \psi_n(\hat{r})$$

$$b = \sum_{n=1}^{m} \frac{(\psi_n, F_\omega)}{\lambda_n^2 + \omega^2} \omega \psi_n(\hat{r})$$

where $|A(\hat{r})|$ and $\alpha(\hat{r})$ are the amplitude and lag of the temperature response to the periodic forcing, respectively.

If the temperature is assumed to be driven by annual-mean forcing $F(\hat{r})$, by (2.1) our annual-mean temperature model can be written as

$$-\nabla \cdot (D(\hat{r})\nabla T(\hat{r})) + A + BT(\hat{r}) = F(\hat{r}) \tag{2.21}$$

Equation (2.21) is a non-homogeneous, linear, second-order ODE. It is straightforward to solve (2.21) numerically (detailed numerical procedures in Appendix B).

Applications of the responses to annual-mean and periodic forcing can be made by setting the appropriate annual-mean and seasonal-cycle forcings for the system. The zonally averaged solar radiation forcing $F_S(y,t)$, which drives the Earth-Atmosphere temperature field, was introduced by North et al. (1979) and North et al (1983). It can be well represented by the combination of the annual-mean, annual-cycle and semi-annual-cycle forcings as

$$F_S(y,t) = Qa(y)S(y,t) \tag{2.22}$$

with

$$a(y) = a_0 + a_2 P_2(y) \tag{2.23}$$

$$S(y,t) = 1 + S_1 \cos(2\pi t) P_1(y) + (S_2 + S_{22} \cos(4\pi t)) P_2(y) \tag{2.24}$$

where

y = the sine of latitude

t = time

Q = a quarter of the solar constant (~340 W/m^2)

$a(y)$ = zonally averaged co-albedo

$S(y,t)$ = solar radiation absorbed

$P_1(y) / P_2(y)$ = the 1st /2nd order Legendre Polynomials: y , $\frac{1}{2}(3y^2 - 1)$

a_0, a_2 = the coefficients for co-albedo function

S_1, S_2, S_{22} = the coefficients for the incident solar radiation function

The solar radiative forcings used in our models are shown in Figure 5.

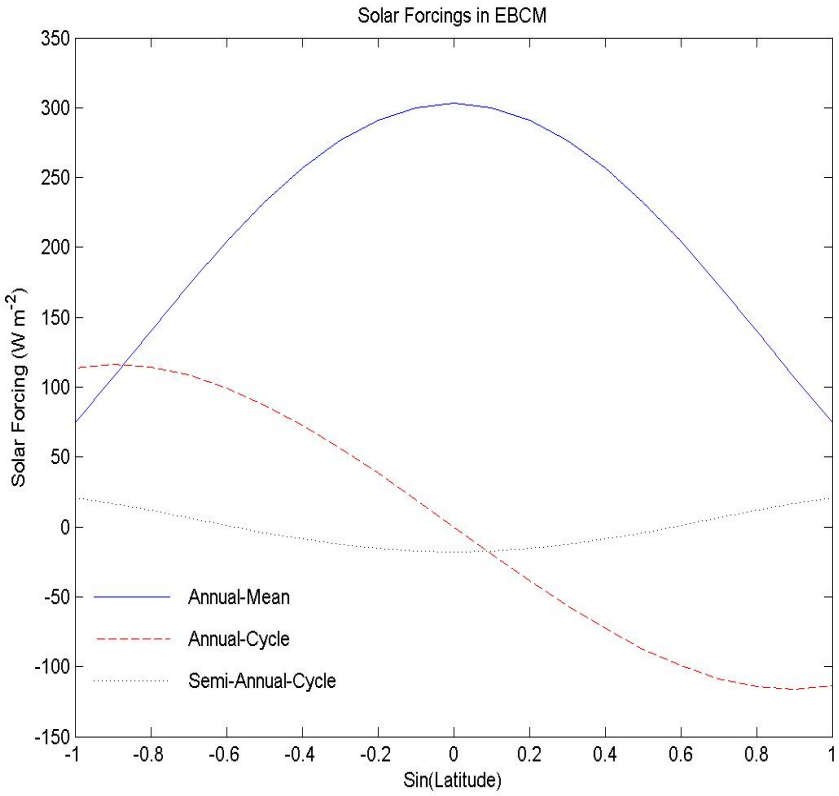

Fig. 5. Solar radiative forcings used in present EBCMs. Blue solid curve is annual-mean temperature, red dashed curve is annual-cycle amplitude, and black dotted line is semi-annual-cycle amplitude.

By substituting (2.23) and (2.24) into (2.22), we can get expressions for the annual-mean, annual-cycle and semi-annual-cycle solar radiation forcings.

The annual-mean and annual-cycle temperature responses were simulated respectively by using (2.21) and (2.20). The results show that the temperature responses to the angular frequencies $\omega = 0,\ \ 2\pi$, 4π were identical to those of the earlier published simulations, such as North et al. (1983). The parameters used in the present

studies are listed in Table 1. The reason of tuning model parameters will be explained in later section 2.7. As a consistency check, we also use the parameters of NMS83 and those of Hyde et al. (1989, 1990) to reconstruct the annual-mean and annual-cycle temperature fields and the results proved to be identical to the previously published

Table 1. Values of model parameters used in the present studies. The horizontal thermal diffusion coefficient depends on latitude through $D(\mu) = D_0(1 + D_2\mu^2 + D_4\mu^4)$ (North et al. 1983) and the co-albedo is $a(\mu) = a_0 + a_2 P_2(\mu)$, where $\mu = \sin(Latitude)$ (North and Coakley 1979).

Parameters	Values Setting
A	184.0 W m^{-2}
B^{land}	2.094 W m^{-2} K^{-1}
B^{ocean}	2 × B^{land}
D_0^{land}	0.505 W K^{-1}
D_0^{ocean}	D_0^{land} /10
D_2	-1.33
D_4	0.67
a_0	0.62
a_2	-0.20
C^{land}	0.1605 W m^{-2} K^{-1} yr
C^{ocean}	3.23 W m^{-2} K^{-1} yr
S_1	-0.796
S_2	-0.477
S_{22}	0.147
Q	340 W m^{-2}

solutions. Hence, the modal expansion method can be used to solve the EBCM, but it is not an especially efficient way of obtaining solutions. The power of the method is the insight it brings and as a potential tool for data analysis and model comparison.

The historical record NCAR $5^o \times 5^o$ combined land and marine monthly temperature anomalies data (Jones dataset) from 1854 through 2002 (available at *http://www.cru.uea.ac.uk/cru/data/)* are used to analyze observational annual-mean and annual-cycle temperature patterns. We chose the latest 25-yr data set for this analysis. Figure 6 shows the amplitude of temperature response to annual-cycle forcing. The strongest response occurs over NH continents. The maximum amplitude of the response is forced over central Eurasia. The observed amplitude of the annual-cycle temperature is presented in Figure 7. The two panels exhibit a surprising resemblance considering the simplicity of the EBCM. Note that this comparison is the same whether the TDMs are used for the solution or whether the conventional techniques are used such as Spherical Harmonics (North et al. 1983; Stevens 1997).

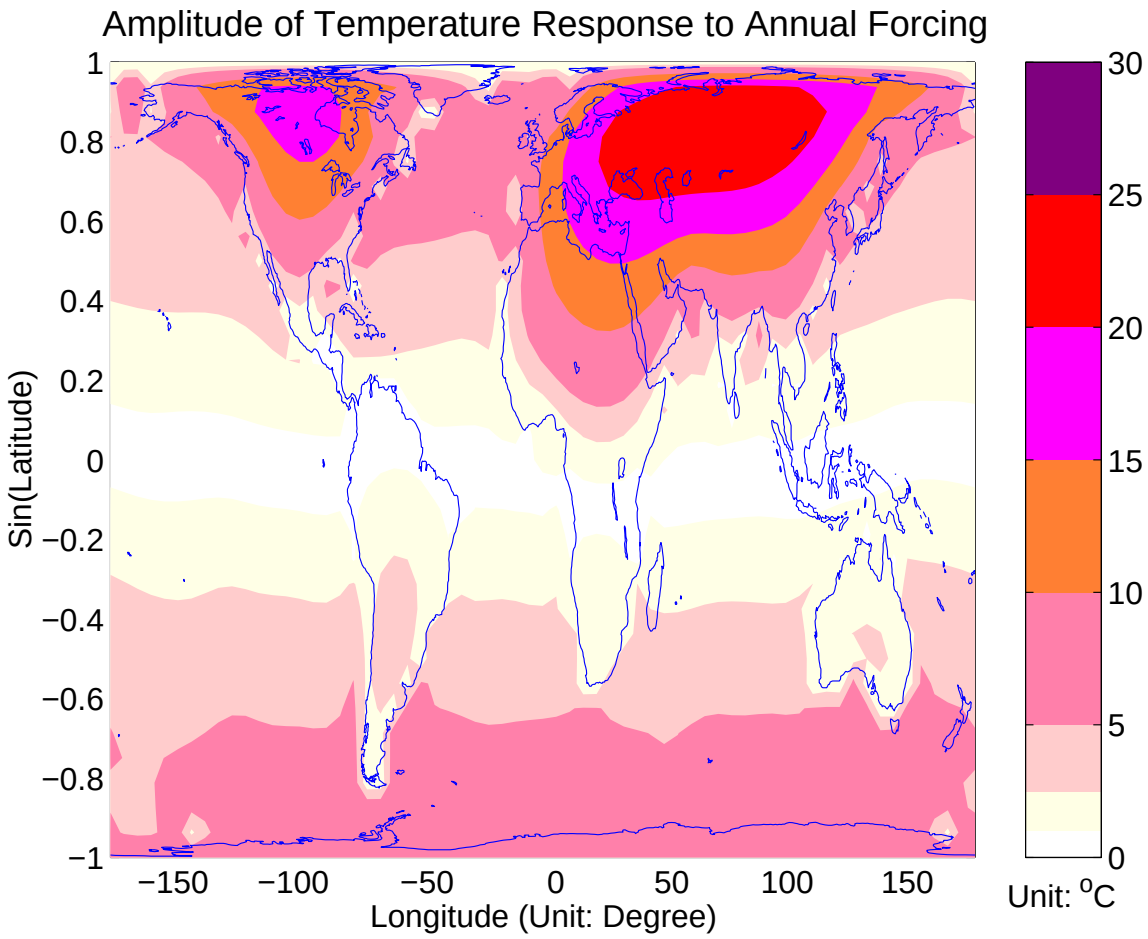

Fig. 6. The amplitude of the temperature response to annual-cycle forcing from the model. Larger response occurs over Northern-Hemisphere continents. The temperature reaches the maximum (~ 25 ^{o}C) over central Eurasia.

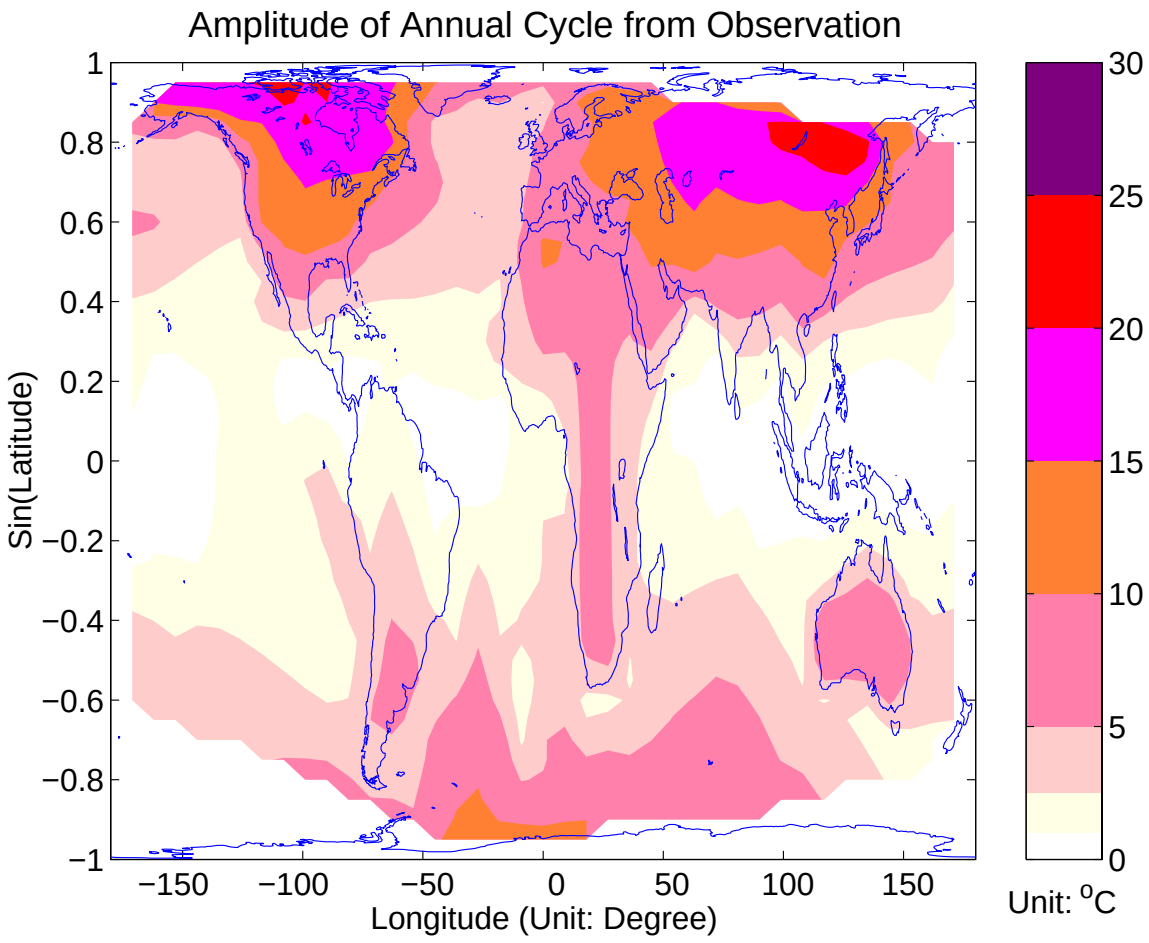

Fig. 7. The amplitude of the annual-cycle temperature from observation. As in Fig.6 but for the observed temperature field. Note that no data is available over the polar regions.

As an example, Figure 8 shows the amplitude of temperature response to annual-cycle forcing by using the model parameters in Hyde et al. 1990. The result gives a very similar pattern to that in Figure 6. The amplitudes in central Eurasia and North America

present the strong response seen in Figure 6. The magnitude of the response is a bit higher than the observations in Figure 7 and the model result shown in Figure 6.

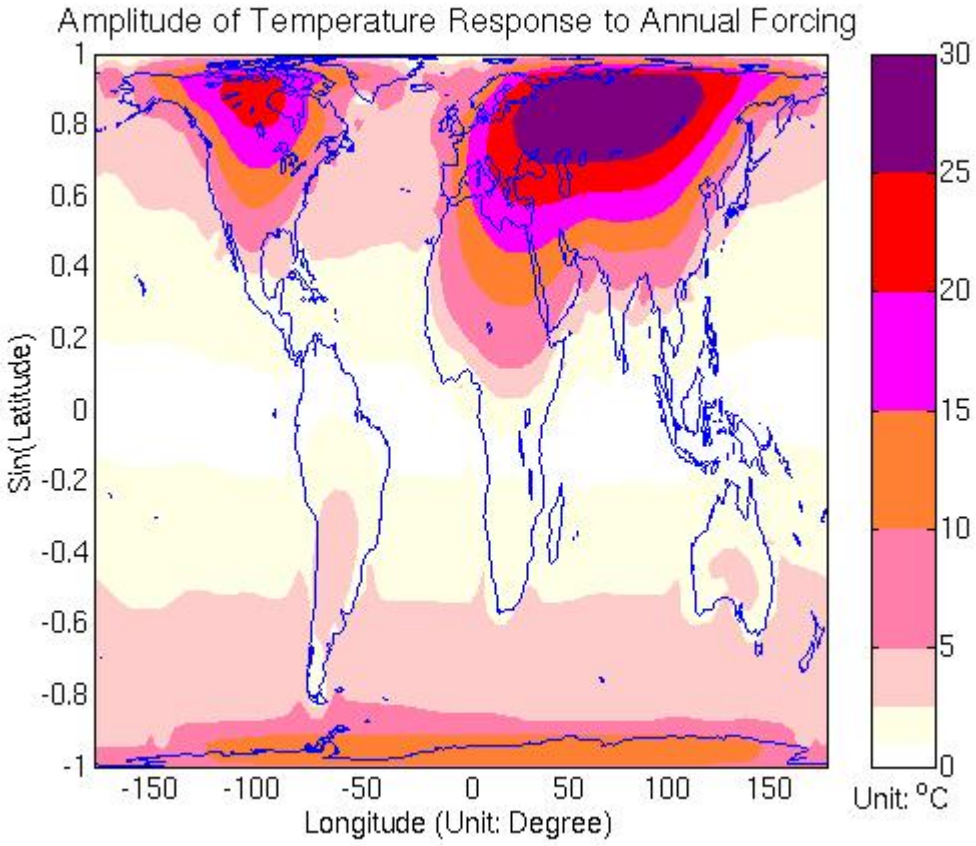

Fig. 8. The amplitude of the temperature response to annual-cycle forcing from the model by using parameters in Hyde et al. 1990. The pattern looks similar to those in Figures 6 and 7 except a little larger temperature over Northern-Hemisphere continents.

The phase lags of modeled and observed annual-cycle temperature are shown in Figures 9 and 10, respectively. The modeled phase lag shows a smaller value over continents with dominant lag intervals of 10 to 30 days, while the observed phase lag is

of order 20 days ~ 40 days. Note that the observed phase lag near the Equator appears noisy and distracting due to the small value of the amplitude of the annual harmonic.

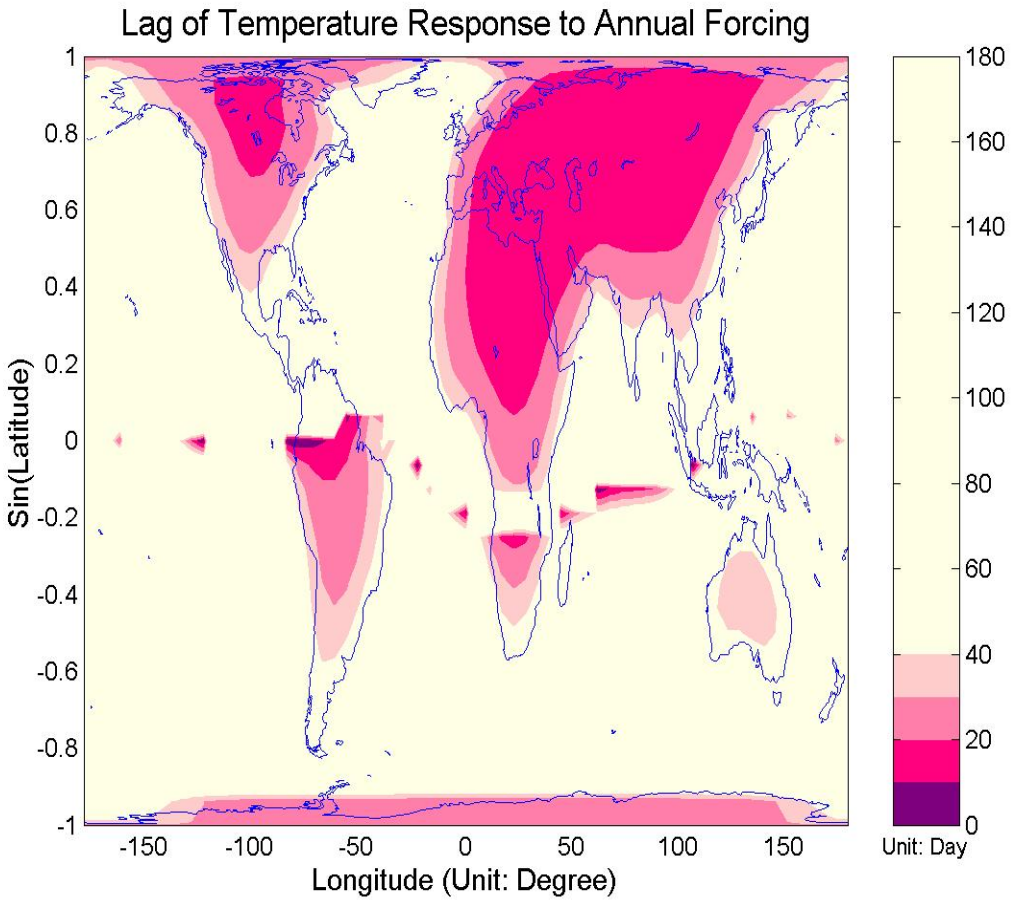

Fig. 9. The lag of the temperature response to annual-cycle forcing from the model. The dominant lags over continents show 10 ~ 30 days.

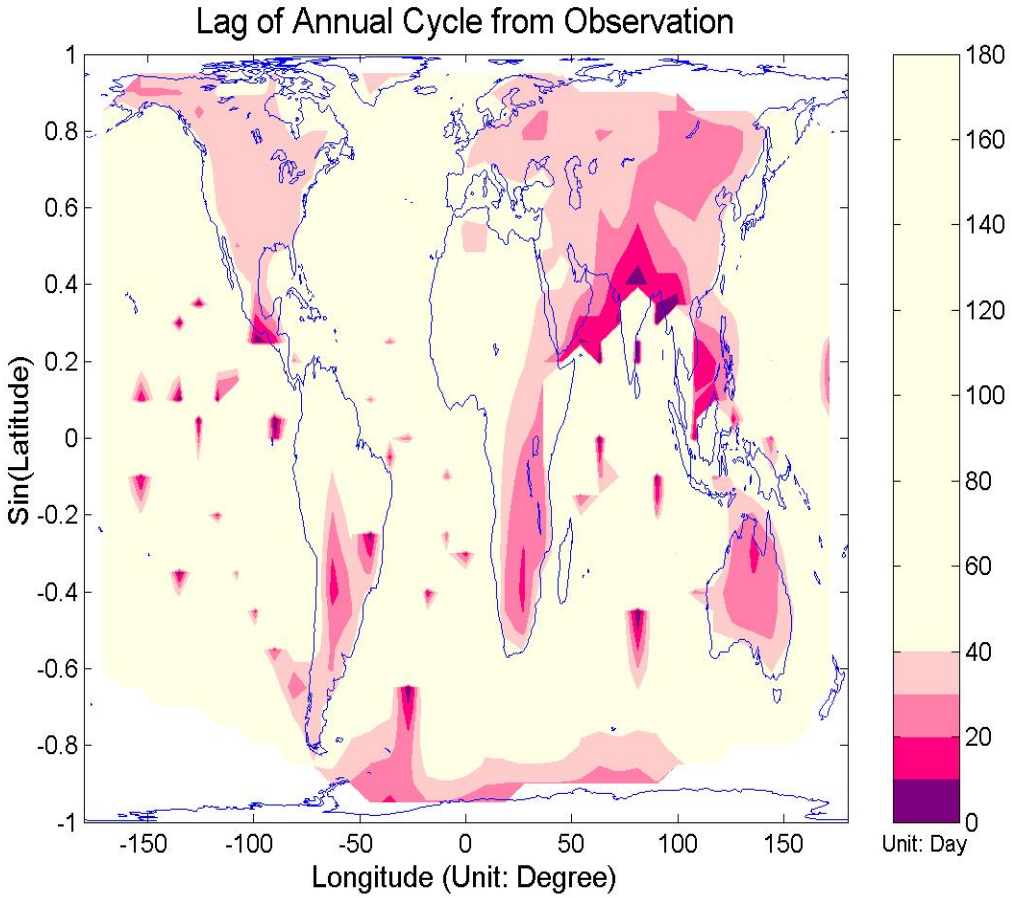

Fig. 10. The lag of the annual-cycle temperature from observation. The dominant lags over continents show 20 ~ 40 days, a bit larger than the model result in Fig. 9. The noisy phase lag near the Equator is due to the small value of the amplitude of the annual harmonic. Note that no data is available over the polar regions.

The amplitudes of the second harmonics for the modeled and observed temperature fields present dominant features also in continental regions (see Figure 11 and Figure 12). The major amplitude of the temperature response to the semi-annual forcing occurs

in the polar regions. The order of the response amplitude is about one tenth that of the annual response.

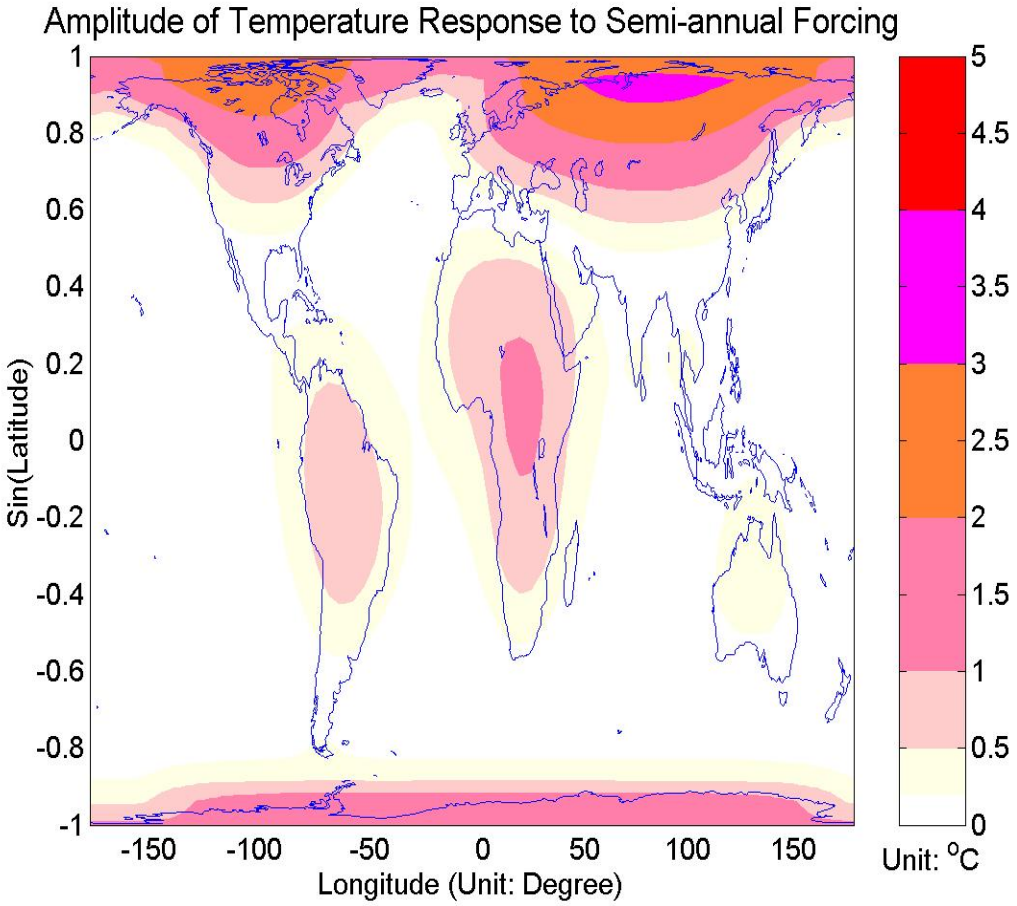

Fig. 11. The amplitude of the temperature response to semi-annual-cycle forcing from the model. Similar to the annual-harmonic case, the dominant amplitude response of the semi-annual harmonic occurs over Northern-Hemisphere continents and near the polar regions, with approximately one-tenth amplitude of the annual-cycle response.

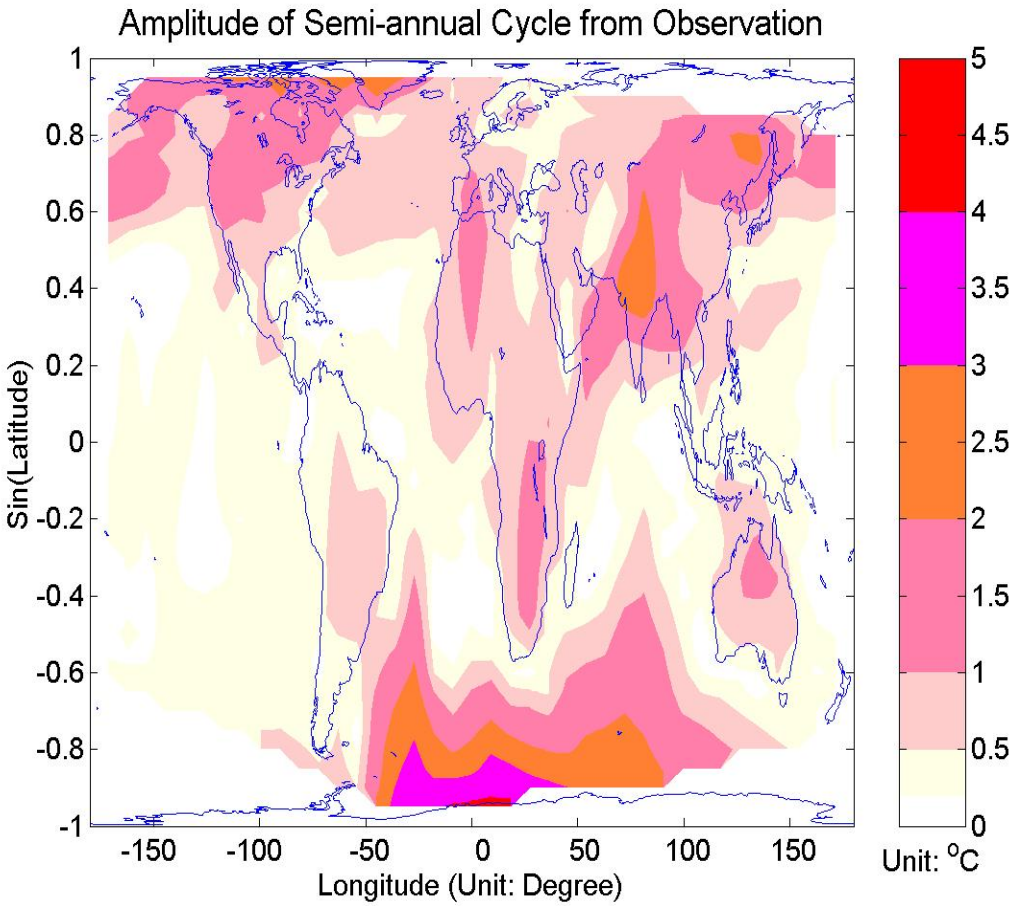

Fig. 12. The amplitude of the semi-annual-cycle temperature from observation. As in Fig. 11 but for the observed temperature field. Note that no data is available over the polar region, and the large values near the South Pole are probably caused by data errors.

Figures 13 and 14 show the modeled and observed annual-mean temperature patterns which are higher near the Equator within 30°S ~ 30°N and decrease towards the poles. The temperature over the oceans captures the dominant feature in the annual-mean temperature field. Figure 15 presents the modeled and observed zonally averaged

annual-mean temperature. The zonally averaged temperature reaches its maximum (close to 30^{o}C) near the Equator. The observed curve shows the flat pattern near the Equator which could be caused by Hadley circulation and strong cloud feedback around the ITCZ and SPCZ regions.

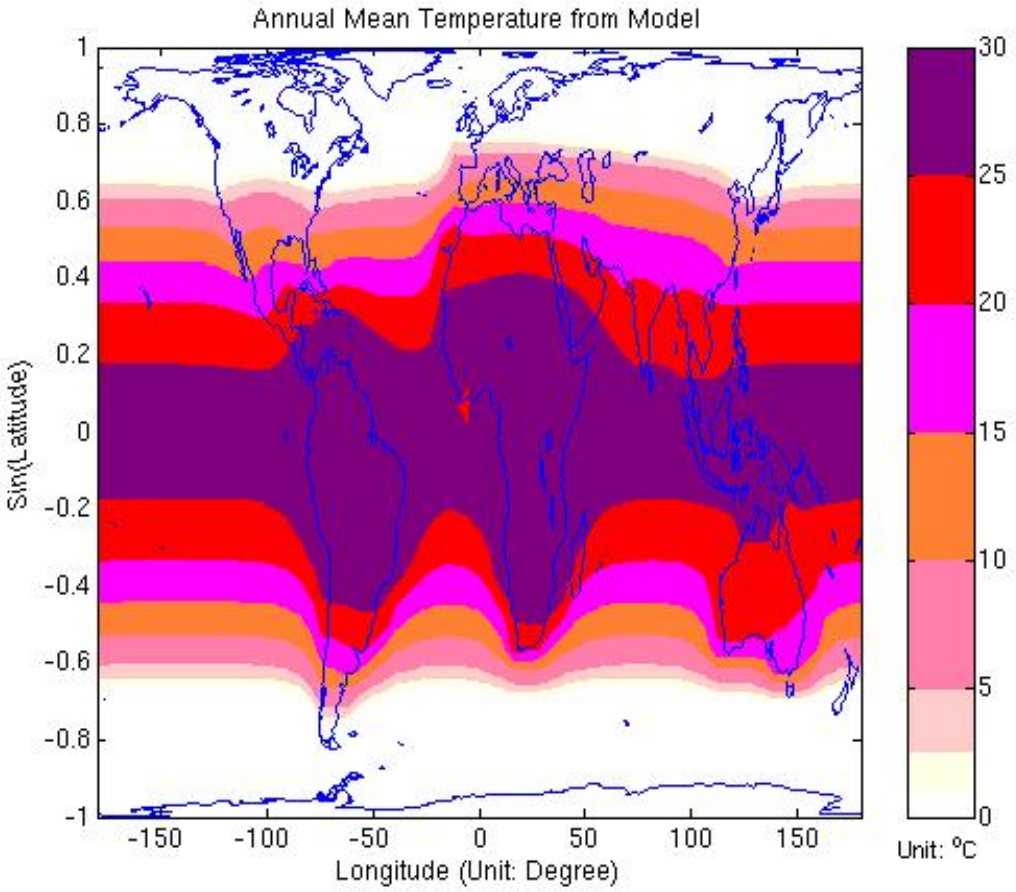

Fig. 13. The temperature response to annual-mean forcing from the model. Larger response occurs near the Equator within 30^{o}S ~ 30^{o}N and then decreases towards the poles. The temperature over the oceans captures the dominant features in the annual-mean temperature response.

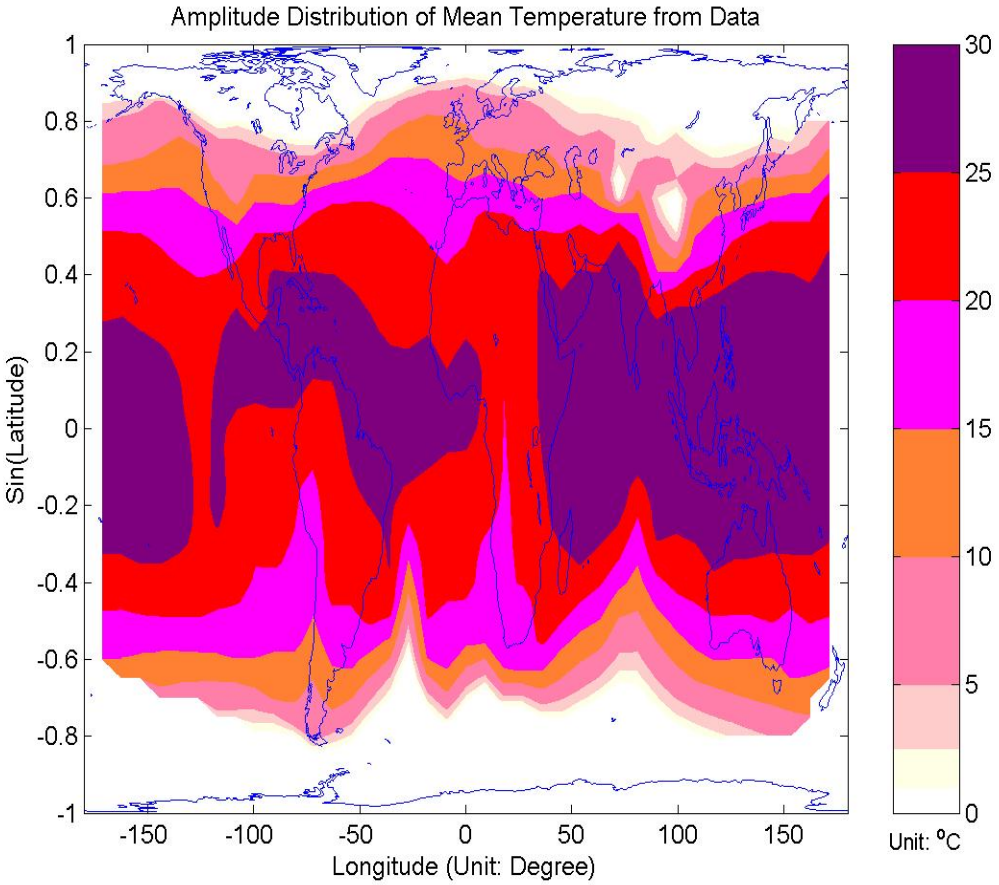

Fig. 14. The annual-mean temperature from observation. As in Fig. 13 but for the observed temperature field.

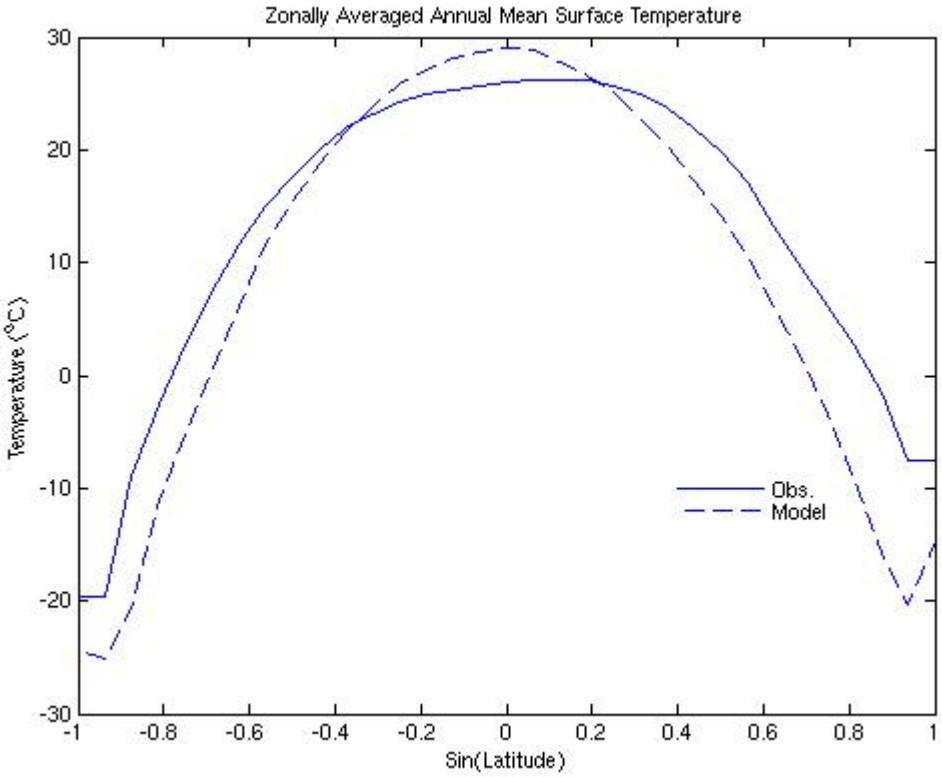

Fig. 15. The zonal averaged annual-mean temperature from model and observation. The solid curve is from observation (Jones dataset). The dashed curve is from the model. The zonal averaged temperature reaches about 30^{o}C near the Equator. The reasons of the near-Equator flatten pattern from observation are probably related to Hadley circulation and strong cloud feedback around the ITCZ and SPCZ.

2.5. Responses to White Noise Forcings

In this section, we will first test the variance of the global surface temperature driven by white-noise forcing, and then examine the autocorrelation time scales for each-

mode amplitude of the surface temperature in response to the weather forcings with 3 different characteristic time scales.

First, we set our external forcing to be white noise in time and space, which can be written as

$$\tilde{F}(\hat{r},t) = \sum_n F_{f_n}(\hat{r}) e^{i2\pi f_n t} \Delta f \tag{2.25}$$

where $F_{f_n}(\hat{r})$ is white noise in space. We represent the temperature response to the noise forcing $\tilde{F}(\hat{r},t)$ is

$$\tilde{T}(\hat{r},t) = \sum_n a_n(t) \psi_n(\hat{r}) \tag{2.26}$$

As we mentioned in 2.2, we have

$$\dot{a}_n(t) + \lambda_n a_n(t) = (\psi_n(\hat{r}), \tilde{F}(\hat{r},t)), \quad n = 1, 2, 3, ... \tag{2.27}$$

where λ_n and $\psi_n(\hat{r})$ are the n -th eigenvalue and eigenmode, $a_n(t)$ is the n -th eigenmode's amplitude of the temperature response.

We can calculate $a_n(t)$ through (2.27) and then plug it into (2.26) to get $\tilde{T}(\hat{r},t)$. For each grid point $\hat{r}$, we can then estimate the variance of the surface temperature as

$$Var(\tilde{T}(\hat{r},t)) = < (\tilde{T}(\hat{r},t) - \overline{T}(\hat{r},t))^2 > \tag{2.28}$$

where <> represents temporal ensemble average.

The variance clearly decreases with frequency increase and so presents a red-noise spectrum to white-noise input. As examples, Figures 16 and 17 present the variance distributions of the response temperature fields for period one month and one year respectively. The variance is large over continents with the dominant feature over

central areas of NH continents. This result agrees with the results from data analysis by Kim and North (1991) and Stevens (1997).

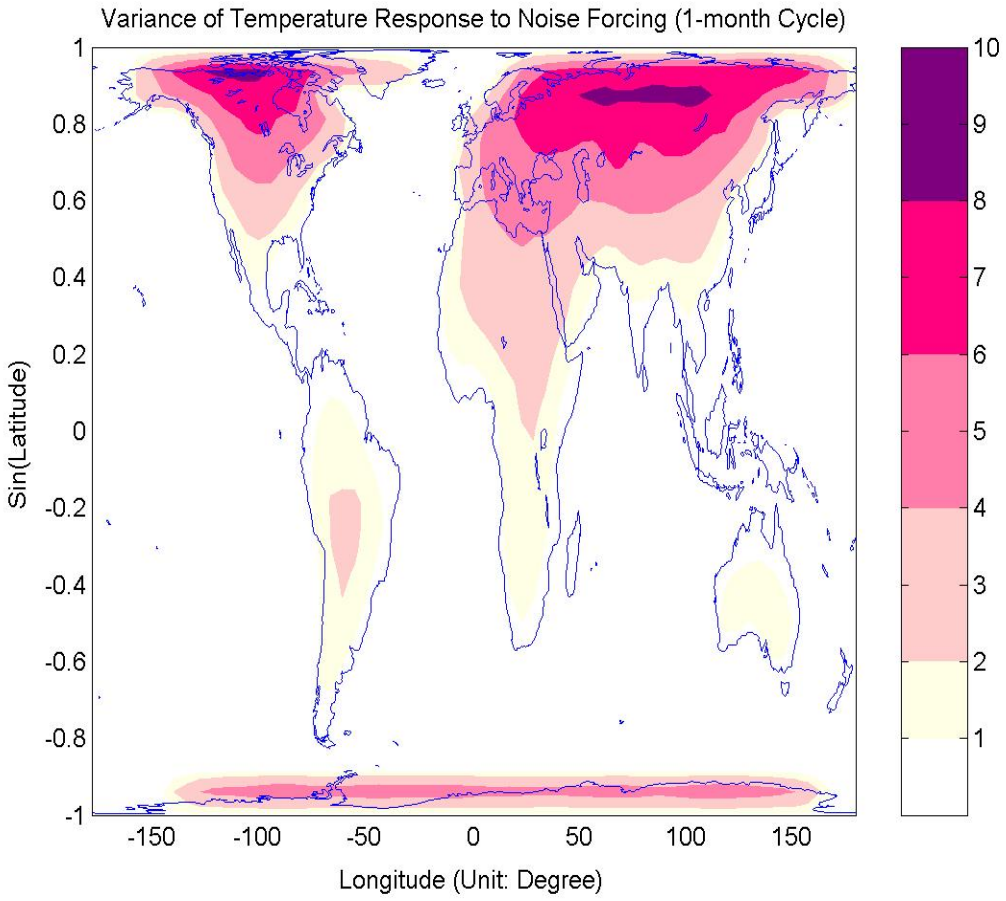

Fig. 16. The variance of temperature response to noise forcing at the one-month period. The large variance occurs over central areas of North-Hemisphere continents. Unit is $(^{o}C)^{2}$.

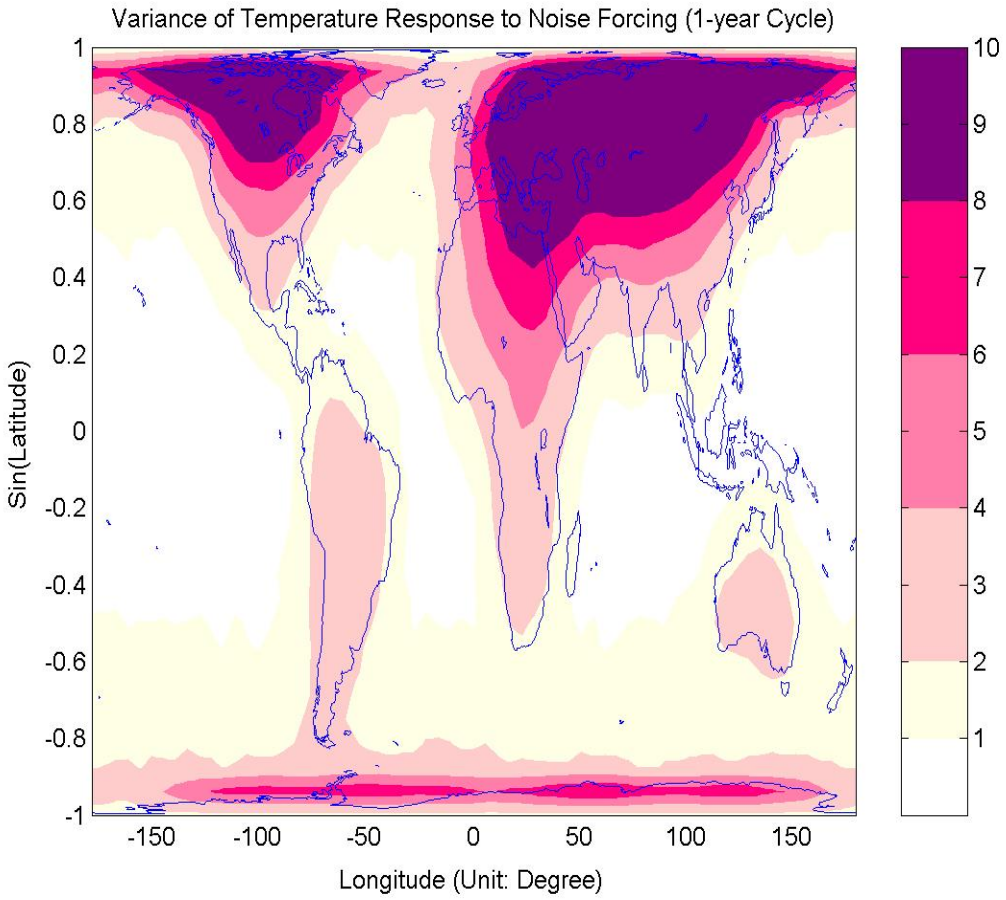

Fig. 17. The variance of temperature response to noise forcing at the one-year period. As in Fig. 16 the large variance occurs over central areas of North-Hemisphere continents but the variance here is much larger with smaller frequency. Unit is $(^{o}C)^{2}$.

2.6. Data Projections

In this section, we project the fluctuating part of observational temperature data onto the modes to create time series of mode amplitudes of fluctuating temperature

$$a_n(t_k) = (\psi_n(\hat{r}), C(\hat{r})\tilde{T}(\hat{r}, t_k)) \tag{2.29}$$

where time-step index k = 1, 2, 3, ..., K. Then we calculate the autocorrelation time scale τ_n through the time series $a_n(t_k)$, t_k =1, 2, 3, ……. . Finally, we compare the autocorrelation time scale τ_n to the theoretical decay time scale $1/\lambda_n$.

Suppose that $\tilde{T}(\hat{r},t)$ is the observed temperature perturbation at point $\hat{r}$ and time t. It can be obtained from the original observational data as

$$\tilde{T}(\hat{r},t) = T^{data}(\hat{r},t) - T^{data}_{mean}(\hat{r}) - T^{data}_{periodic}(\hat{r},t) \tag{2.30}$$

where $T^{data}(\hat{r},t)$ is the observed temperature data, $T^{data}_{mean}(\hat{r})$ and $T^{data}_{periodic}(\hat{r},t)$ represent the annual-mean signal and the periodic signals in the data $T^{data}(\hat{r},t)$.

The 20-yr (1983 to 2002) daily near surface air temperature data, which can be obtained from the NCEP daily reanalyzed dataset (available at *http://www.cdc.noaa.gov/*), are used to analyze the autocorrelation time scales of land modes. This daily air temperature dataset is not appropriate for ocean-mode analysis because it is not able to represent the mean temperature of the ocean mixed layer. So we chose the 21-yr (1981-2001) NCEP reanalyzed weekly averaged surface temperature data for the autocorrelation analysis of ocean modes, since the ocean data are complete for this period. The weekly data are not able to be used for the analysis of land modes which have decay time scales of a few days. The data represent an average temperature from 5 to 10 m depth over ocean. We removed the trends and the seasonal cycle first and then did the projections onto each mode pattern to obtain the time series of mode amplitudes $a_n(t_k)$, t_k =1, 2, 3, ……. . Then we calculated the autocorrelation functions

of $a_n(t_k)$ to estimate the autocorrelation time scales τ_n. The results are shown in Figure 18 as the dotted line.

The three log-log spectra of decay times in Figure 18 are presented as a function of mode index n. The dashed line is the spectrum of the theoretical mode decay times by using the parameters in Hyde et al. 1990. This curve is strongly sloped downwards as a function of log n. The dotted line is the spectrum of the estimated autocorrelation time scale of the mode amplitude time series produced from data projections. These values appear to be noisy partly because there is an ambiguity in the index label for these modes, because any linear combination of the eigenfunctions with the same eigenvalue can also be an eigenfunction. The spectrum of these estimated autocorrelation time scales is clearly flat over ocean modes with about a 2~3-month time lag, which implies that the ocean modes are statistically independent of one another and therefore they are close to white noise in space. For this reason, we adjusted the parameters over ocean to make the length scale of the oceans in the model much shorter than in earlier studies. The local length scale can be expressed as $l(\hat{r}) = \sqrt{\frac{D(\hat{r})}{B(\hat{r})}}$ (North et al 1981). So either reducing $D(\hat{r})$ or increasing $B(\hat{r})$ shortens $l(\hat{r})$. They are both meaningful from a physical point of view because the Rossby Radius $Ro(\hat{r}) = \frac{\sqrt{g'(\hat{r}) * H(\hat{r})}}{f}$ ($g'(\hat{r})$ is a reduced gravity, $H(\hat{r})$ is a layer thickness, f is the Coriolis parameter) (Gill 1982) is about ten times lower over the oceans than in the atmosphere considering in the mid latitude, moreover $B(ocean)$ should be increased if we consider the heat leakage to/from

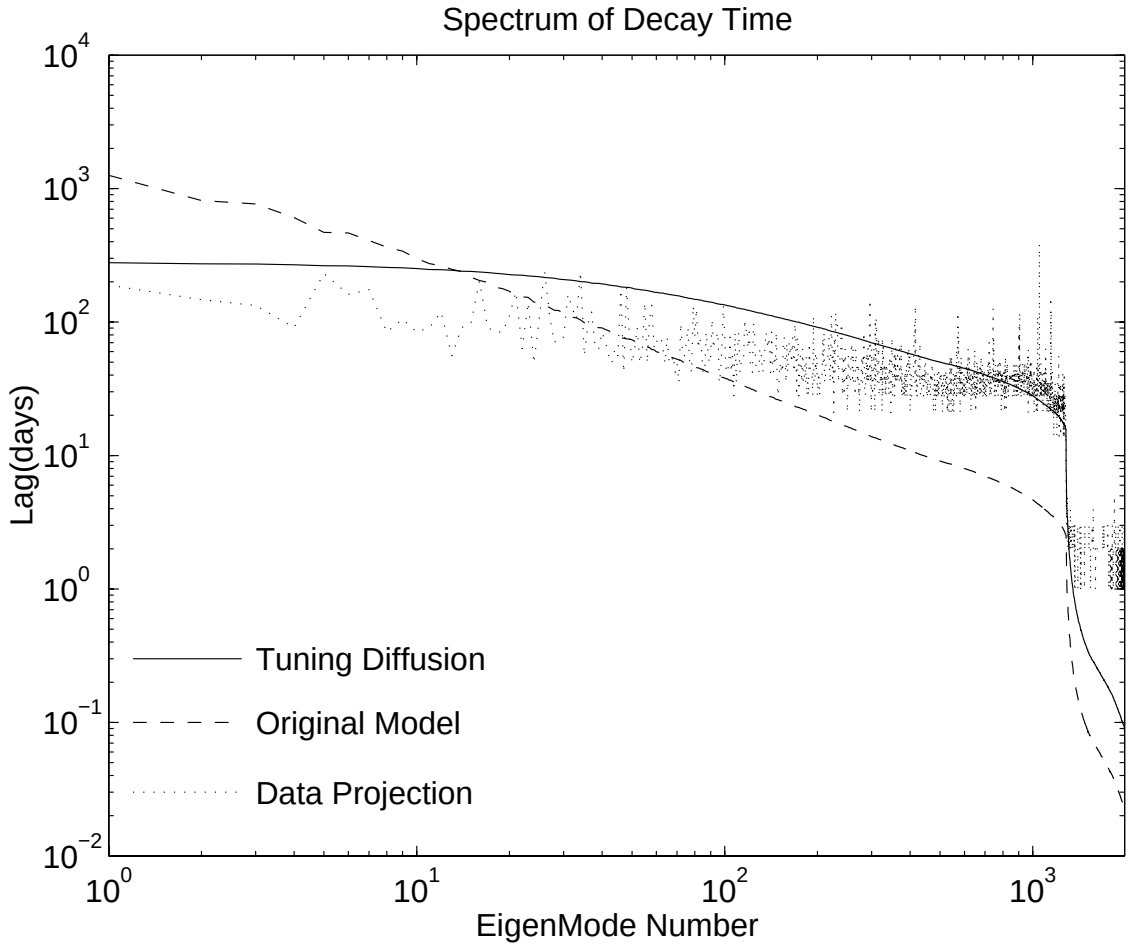

Fig. 18. Log-log spectra of decay time scales as function of mode index n. The dashed line is the spectrum of theoretical decay time scales from older EBCMs. The dotted line is the spectrum of the estimated autocorrelation time scales from data projections onto the TDMs. The solid line is the spectrum of theoretical decay time scales from the tuned model with much shorter length scales over the oceans.

the ocean mixed layer to layers below. The theoretical decay time scales from the tuned model can capture the basic properties of the modal autocorrelation time scales from data projections even though they do not match perfectly. Note that the flat spectrum of the estimated autocorrelation time scales over land modes is due to the resolution of the daily data. That means that the land-mode autocorrelation time scales of less than one day are too short to be solved by data projection. As we mentioned before, the tuned model reconstructs identical solutions for annual-mean, annual-cycle and semi-annual-cycle surface temperature (see section 2.4).

2.7. Remarks on Autocorrelation Function of Mode Amplitudes

Autocorrelation functions of mode amplitudes by data projection are compared with mode's decay time scales in this section. These autocorrelation functions show interesting exponential decay patterns for most of the modes. Figures 19, 20 and 21 present the autocorrelation functions of the first 36 land modes. The predominant feature of these patterns is that observed modal autocorrelation time scales are comparable to theoretical modal decay time scales. It implies the existence of these modes in nature and their very short dissipation time scales. The patterns of the first 36 ocean modes are shown in Figures 22, 23 and 24. Similar properties are exhibited in these figures except the ocean modes present longer time scales ~ 2-3 months.

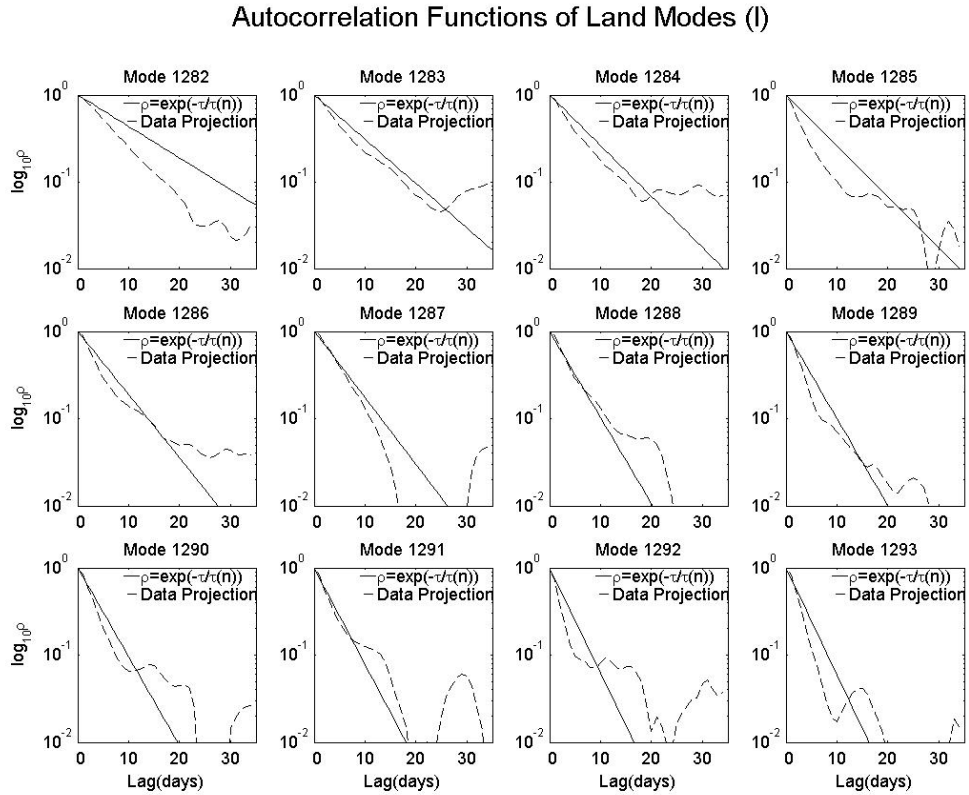

Fig. 19. Autocorrelation functions of the 1st 12 land modes. Note that some autocorrelation functions of mode amplitudes by data projection show not only the exponential decay pattern but also clear periodic signals, e.g., signals with ~30-day period in modes 1287, 1290 and 1291. It indicates that the fluctuating part of the data is contaminated by some periodic signals. The same is for the other autocorrelation figures in the following.

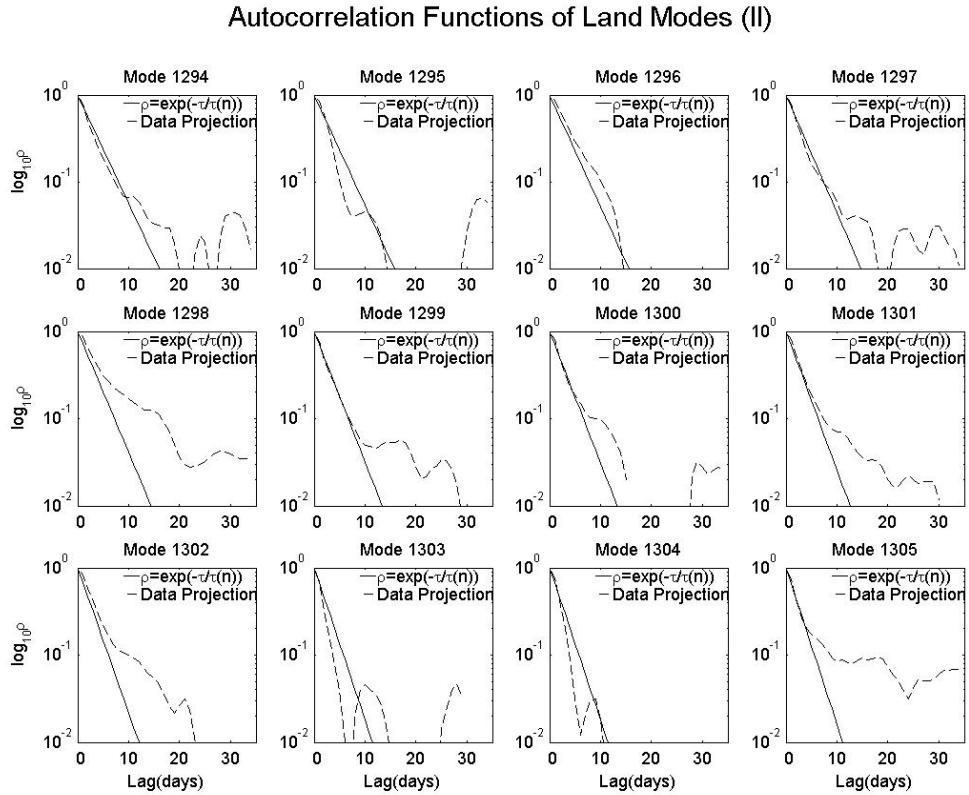

Fig. 20. Autocorrelation functions of the 2nd 12 land modes. As in Fig. 19, some periodic signals are clear to see in some of these patterns.

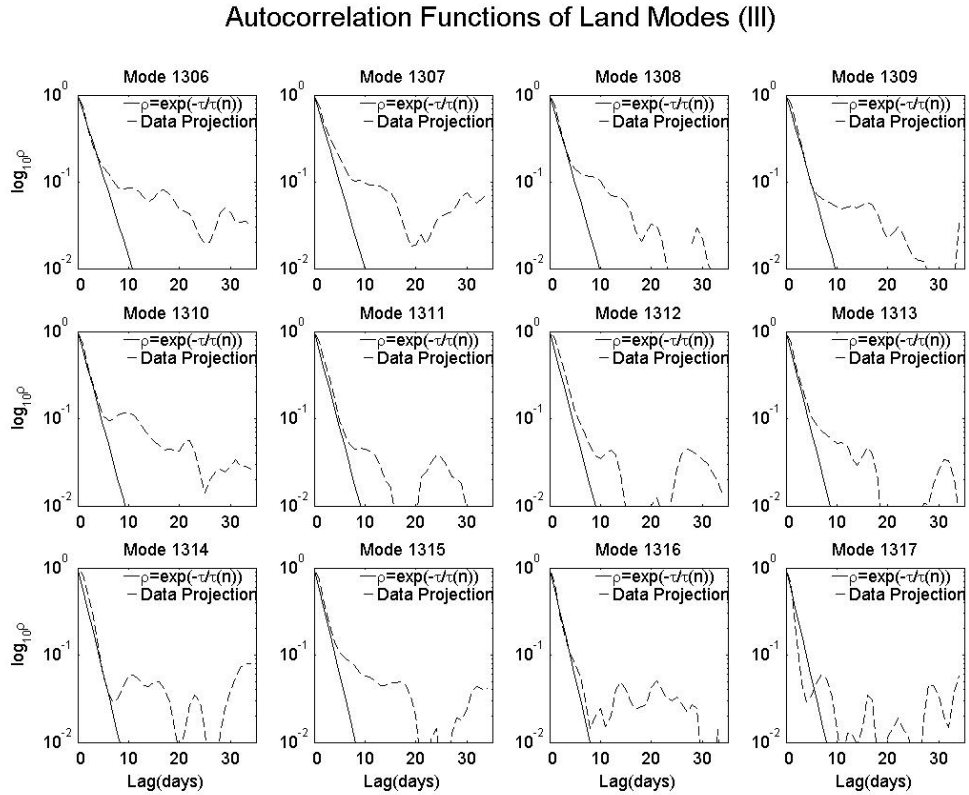

Fig. 21. Autocorrelation functions of the 3rd 12 land modes. As in Figures 19 and 20, some periodic signals are clear to see in some of these patterns.

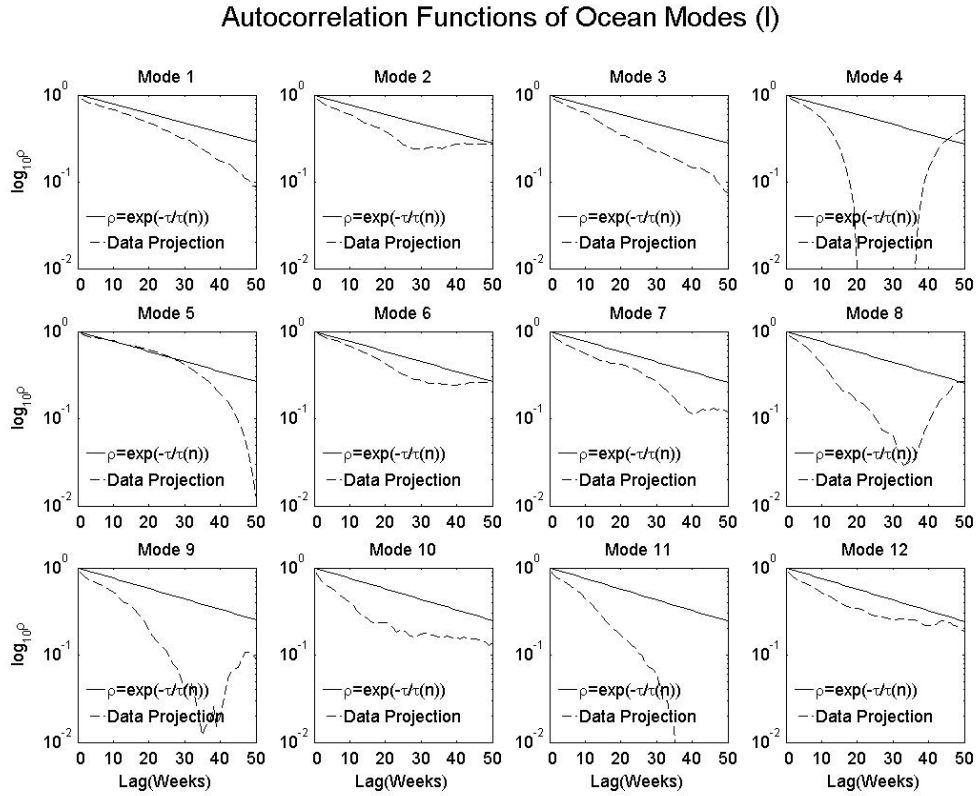

Fig. 22. Autocorrelation functions of the 1st 12 ocean modes. Similar to the land modes in Figures 19, 20 and 21, some periodic signals are clear to see in some of these patterns (e.g., ~ 2-yr-period sub-harmonic signal in mode 11).

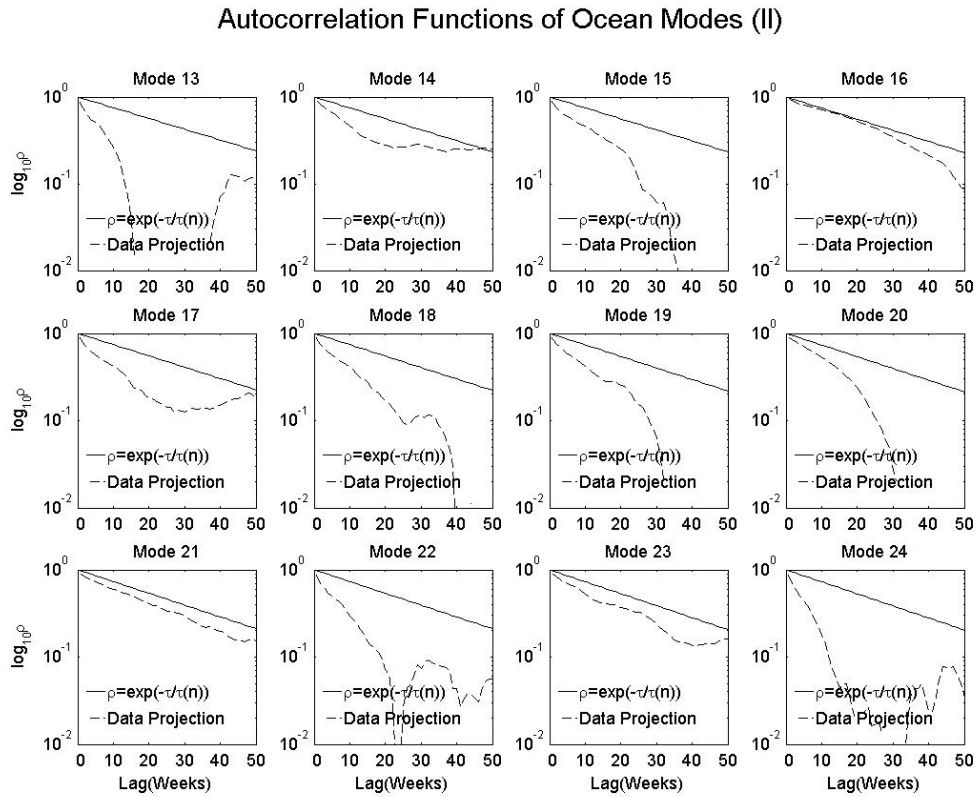

Fig. 23. Autocorrelation functions of the 2nd 12 ocean modes. As in Fig.22, some periodic signals are clear to see in some of these patterns.

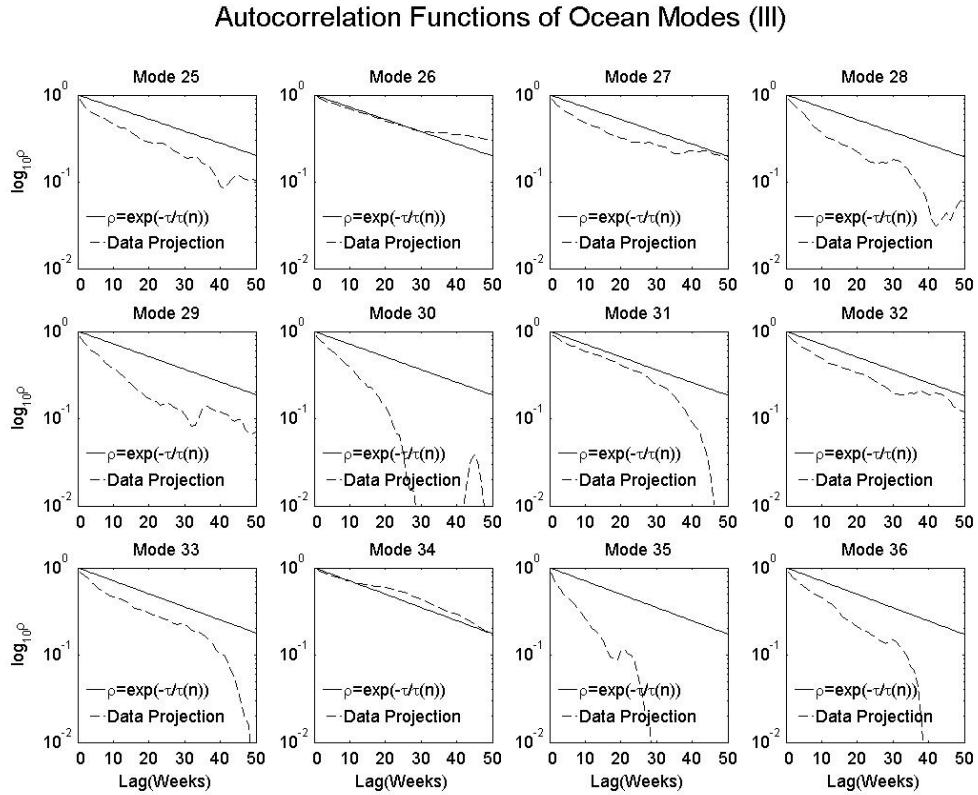

Fig. 24. Autocorrelation functions of the 3rd 12 ocean modes. As in Figures 22 and 23, some periodic signals are clear to see in some of these patterns.

2.8. Summary

Spectral properties of global surface temperature are explored here by generating a complete non-orthogonal series of thermal decay modes. These modes are spatial physical modes with family-style geographic properties. They are useful in reconstructing seasonal variations and examining climate responses to noise forcings. The decay time scales of the modes (2~3-month for ocean modes and ~ a few days for land modes) are important. They indicate how long the thermal energy dissipation will take in surface

temperature fluctuations. These modes in principle need only be solved once for all time dependent linear problems.

The comparable time scales of autocorrelation of modal amplitudes with data projection of mode's decay time scale is comforting. It implies that these decay modes may be a useful complete basis set related to surface temperature fluctuations. The exponential decay pattern of the mode's autocorrelation functions produced by data projection and their similiarity to the decay slopes to the theoretical ones further support the existence of these modes in nature.

The projection of AOGCM output onto these modes may prove to be a useful way of examining the modal decay time scales. Such a test could help in finding which models perform best in their thermal fluctuation decay behavior.

CHAPTER III

PROBABILITY DENSITY FUNCTIONS OF CLIMATE SENSITIVITY

3.1. Introduction

Climate sensitivity is nominally indicated by the steady-state change in globally and annually averaged temperature for a doubling of the concentration of CO_2 in the atmosphere. It has unit of $^{o}C\ (W\ m^{2})^{-1}$. The climate sensitivity depends on a variety of fast radiative feedback processes such as water vapor feedback and cloud feedback by adding to or subtracting from the initial radiative perturbation (Harvey 2000). It is a key determinant of climate change (Hansen et al 1985; Morgan and Keith 1995; IPCC 2001; Frame et al. 2005) but remain largely uncertain in recent climate studies (e.g., Andronova and Schlesinger 2001; Allen and Ingram 2002; Forest et al. 2002; Knutti et al. 2002; Gregory et al. 2002; Stott and Kettleborough 2002; Murphy et al. 2004; Stainforth et al. 2005; Wigley et al. 2005; Frame et al. 2005).

The sensitivity is generally expected to lie between 1.5 ^{o}C and 4.5 ^{o}C (IPCC 2001). This broad range is derived from the values reported by different climate modeling groups around the world and is possibly due to the differences in parameterizations used by different research groups. Recent studies (Andronova and Schlesinger 2001; Forest et al. 2002; Knutti et al. 2002; Gregory et al. 2002; Murphy et al. 2004; Stainforth et al. 2005) attempting to constrain climate sensitivity by different models and present observations, report a wide range of the sensitivity. Frame et al.

(2005) demonstrates that any probabilistic estimate of climate sensivity is critically dependent on subjective prior assumptions of the investigators. Therefore, it seems impossible to get a universal consensus on long-term equilibrium warming consistent with any given stabilization level for greenhouse gases.

In this chapter, we will demonstrate our point of view on the causes of the uncertainties of climate sensitivity. This view is derived from a family of simple energy balance climate models (North et al. 1983) with only a small number of phenomenological coefficients. These models include the most relevant physical mechanisms in a very simple way, allowing straightforward interpretations. We first perturb our four key model parameters A, B, C, D to create a so-called multiple perturbed physical ensemble (PPE) (Murphy et al. 2004) of O(10^6) model versions, each used to simulate global geographically dependent annual-mean and annual-cycle surface temperature field. Then we use the model results to calculate the magnitudes of the errors of modeled temperature fields as referred to observed temperature fields. We proceeded to obtain optimal estimates of the model parameters based on the minimum errors. The probability density functions (PDFs) for the sensitivity under different error tolerance variances were then estimated under a Gaussian statistical assumption. A scheme to objectively estimate the PDF of the climate sensitivity constrained by fit to the present climate was therefore explored in this study.

3.2. Deriving the PDF of Climate Sensitivity

We start with the EBCM (North et al. 1983) as described in Chapter II (2.1). As we previously described, it is a model to simulate the surface temperature as a function of position on the globe $\hat{r}$ and the time of year t. The principle is to balance the energy fluxes entering and leaving a column of the Land-Ocean-Atmosphere system over a single square meter. These fluxes are parameterized in terms of surface temperature and are depicted in the energy balance equation (3.1). Details about this model are described in Chapter II. The governing equation of the EBCM can be written as

$$C(\hat{r})\frac{\partial T(\hat{r},t)}{\partial t} - \nabla \cdot (D(\hat{r})\nabla T(\hat{r},t)) + A + BT(\hat{r},t) = Qa(y)S(y,t) \tag{3.1}$$

where $T(\hat{r},t)$ represents the surface air temperature over land and the mixed-layer temperature over ocean, y is the sine of latitude, $C(\hat{r})$ is the local effective heat capacity (large over ocean, small over land), Q is the solar constant divided by four, $D(\hat{r})$ is a latitude-dependent macroturbulent heat diffusion coefficient, $A+BT$ is nominally the outgoing terrestrial radiation to space. The co-albedo has a latitude dependence decreasing toward the poles (North et al. 1981)

$$a(y) = a_0 + a_2 P_2(y) \tag{3.2}$$

The seasonal distribution of solar insolation can be written as (North et al. 1981)

$$S(y,t) = 1 + S_1 \cos(2\pi t)P_1(y) + (S_2 + S_{22}\cos(4\pi t))P_2(y) \tag{3.3}$$

where $P_n(y)$ is the n th Legendre Polynomial. The latitude dependence of $D(\hat{r})$ is parabolic in y larger at the equator and diminishing toward the poles (Table 1). A natural length scale in the model is given by $\sqrt{D/B}$ (North 1984(b)). The scale of both

D and B are different over ocean and land enabling a smaller length scale over ocean areas (factor of 3.2; see previous chapter). The parameters A, B, C and the overall scale of D (but not its shape) are chosen to be the random variables in our experiments.

As introduced in 3.1, climate sensitivity refers to equilibrium temperature increase due to a doubling of the concentration of CO_2 in the atmosphere. The globally and annually averaged temperature $\overline{T}$ can be derived from equation (3.1) as

$$A + B\overline{T} = Qa_0 \tag{3.4}$$

For the case of doubling CO_2, the globally and annually averaged temperature will increase as a result of the greenhouse effect (Gill 1982). Thus the governing equation for the new equilibrium system can be written as

$$(A + \Delta A_{2\times CO_2}) + B(\overline{T} + \Delta\overline{T}_{2\times CO_2}) = Qa_0 \tag{3.5}$$

Note that $\Delta A_{2\times CO_2} < 0$ (by (3.11)). By subtracting (3.4) from (3.5), we get the sensitivity expression in this model as

$$\Delta\overline{T}_{2\times CO_2} = \frac{-(\Delta A)_{2\times CO_2}}{B} \overset{set}{=} \chi \tag{3.6}$$

where $\Delta A_{2\times CO_2}$ is known (see (3.11)), χ represents the sensitivity. Note that the PDF of sensitivity in this simple EBCM will just be related to the PDF of $1/B$.

If we assume B is a uniformly or normally distributed random variable $\{x\}$, χ is also a random variable. We set $\chi = \{y\} \overset{(3.6)}{=} \{\frac{-(\Delta A)_{2\times CO_2}}{x}\}$. Then we can easily derive the PDF of χ, which is proportional to $1/\chi^2$ shown in the following.

$$F_\chi(y) = P_\chi\{\chi < y\} = P_B\{B > x\} = \int_x^\infty p_B(x)dx = \int_{\frac{-(\Delta A)_{2\times CO_2}}{y}}^\infty p_B(x)dx \tag{3.7}$$

So,

$$p_\chi(y) = \frac{dF_\chi(y)}{dy} = -p_B(\frac{-(\Delta A)_{2\times CO_2}}{y})\frac{d}{dy}(\frac{-(\Delta A)_{2\times CO_2}}{y}) = p_B(\frac{-(\Delta A)_{2\times CO_2}}{y})(\frac{-(\Delta A)_{2\times CO_2}}{y^2}) \tag{3.8}$$

If we assume that B is a uniformly distributed random variable { x }, then

$$p_B(x) = \frac{1}{B_{\max} - B_{\min}}, \quad \text{for } B_{\min} \le x \le B_{\max} \tag{3.9}$$

(zero for other x)

If we assume that B is a normally distributed random variable { x },

$$p_B(x) = N(B_{\min}, B_{\max})e^{-\frac{(x-x_0)^2}{2\sigma^2}}, \quad \text{for } B_{\min} \le x \le B_{\max} \tag{3.10}$$

(zero for other x)

The PDF of climate sensitivity χ by simple EBCM (3.6) is shown in Figures 25 or 26 if we assume B having inverse uniform or normal distribution, respectively. Figures 25 and 26 show highly skewed patterns towards the infinite χ. In this case the mean value of the sensitivity can be quite large if the prior distribution of B is allowed to be finite for small values of B. Hence, the mean value of χ is highly sensitive to the prior distribution of the parameter B.

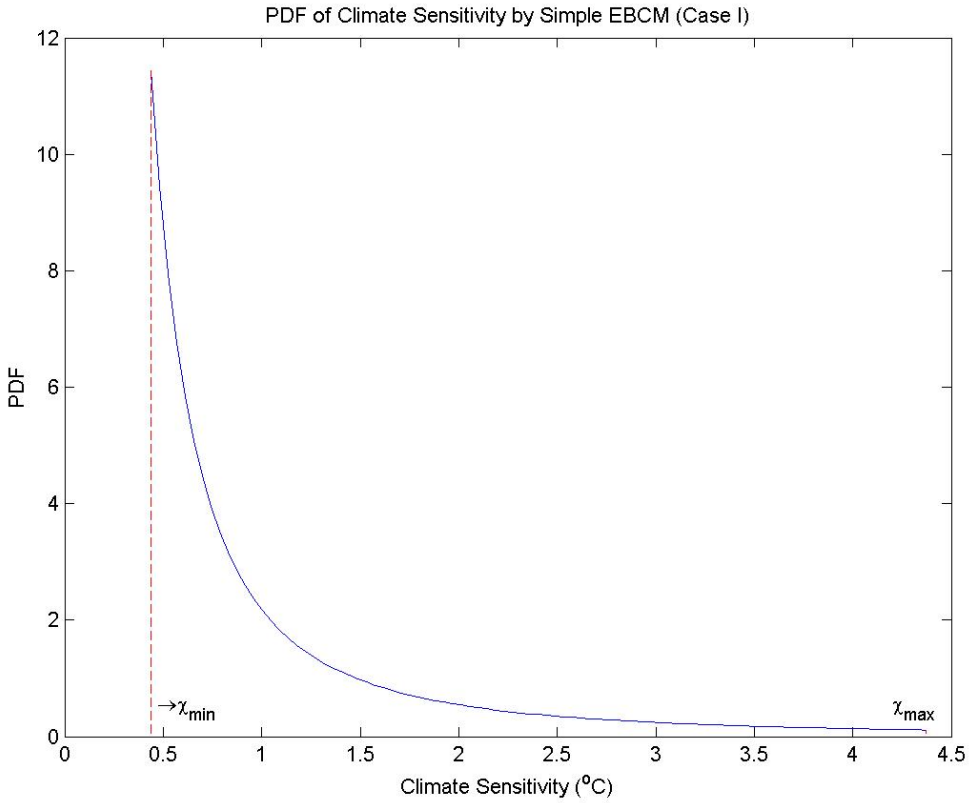

Fig. 25. PDF of climate sensitivity by globally and annually averaged EBCM if B satisfies the uniform distribution. Here $\chi_{\min} = \dfrac{-(\Delta A)_{2\times CO_2}}{B_{\max}}$ and $\chi_{\max} = \dfrac{-(\Delta A)_{2\times CO_2}}{B_{\min}}$.

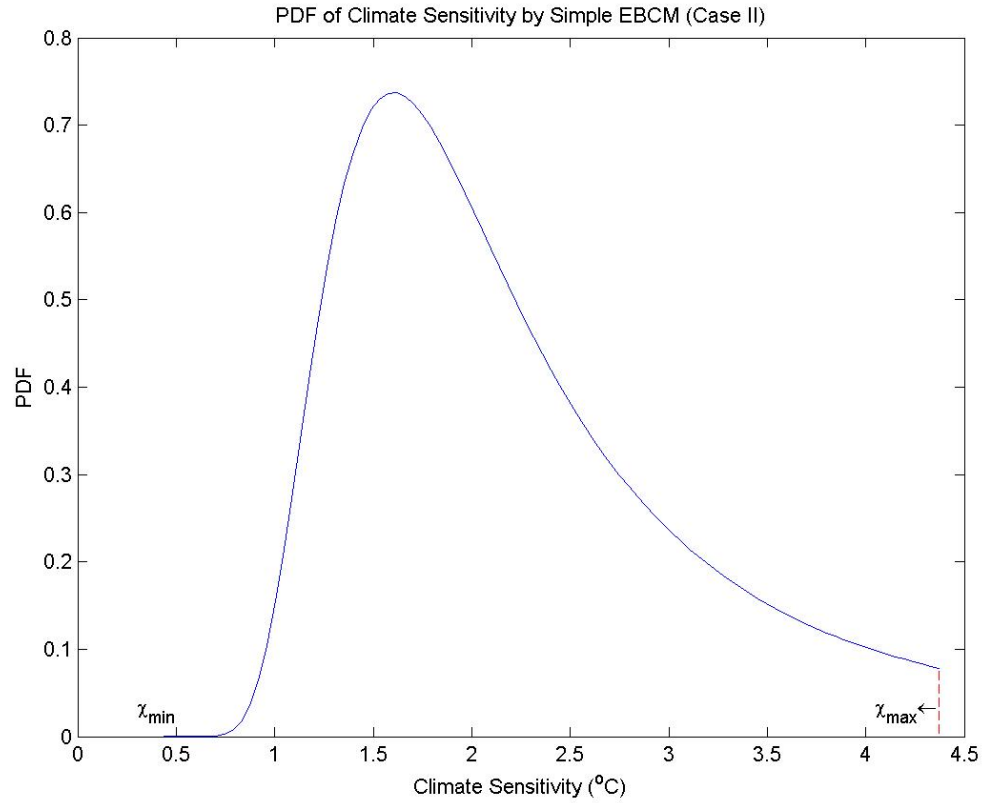

Fig. 26. PDF of climate sensitivity by globally and annually averaged EBCM if B satisfies the normal distribution. Here $\chi_{\min} = \dfrac{-(\Delta A)_{2\times CO_2}}{B_{\max}}$ and $\chi_{\max} = \dfrac{-(\Delta A)_{2\times CO_2}}{B_{\min}}$.

The reduction in A (outgoing radiation) is related to a doubling CO_2 and can be expressed by the formula (IPCC 1990)

$$(\Delta A)_{2\times CO_2} = -\frac{4.37\mathrm{Wm}^{-2}}{\ln 2}\ln\frac{(CO_2)_t}{(CO_2)_0} \tag{3.11}$$

where the subscripts denote concentrations at times zero and t. In this simple formulation stratospheric adjustments are not considered and some of them can enhance

the sensitivity. So our sensitivity may be a little less than in some more comprehensive models (Harvey 2000).

An objective means to estimate the PDF of the climate sensitivity χ constrained by fit to the present climate is introduced here. First, we perturbed the model parameters A, B, C, D to calculate the annual-mean, annual-cycle and semiannual-cycle surface temperatures for different model versions. Then we computed the mean squared errors of modeled and observed temperatures by

$$\varepsilon^2(A,B,C,D) = \int_0^1 \int \{T_{model}(\hat{r},t;A,B,C,D) - T_{data}(\hat{r},t)\}^2 d\hat{r}dt \tag{3.12}$$

This is a measure of the goodness of fit for the modeled seasonal climate to the observed seasonal climate, which is integrated over the globe and through the year. For a given group of parameters A, B, C, D, we obtain a single realization of the independent random variables.

We produce a likelihood-weighted PDF of climate sensitivity by constraining the modeled temperature to the observations through the mean square error depicted above. We assume a prior distribution $p(A,B,C,D)$ to be expressed as

$$p(A,B,C,D)dAdBdCdD = Ne^{\frac{-\varepsilon^2(A,B,C,D)}{2\sigma^2}} dAdBdCdD \tag{3.13}$$

The parameter σ is a tolerance level of error. It is a free parameter and represents the error we are willing to tolerate in the fit of the model to the observations. N is a normalization constant.

The marginal PDF for the sensitivity is $p(\chi)$. It may be obtained by transforming the variable B to $1/B$ from (3.13) and then integrating over A, C, D, i.e.,

$$p(\chi)d\chi = \iiint p(A, \chi, C, D)dAdCdDd\chi = \iiint p(A, B, C, D)\left|\frac{dB}{d\chi}\right|dAdCdDd\chi \qquad (3.14)$$

The values of A, B in previous EBCM studies have been taken from terrestrial radiation correlations with satellite data (Graves et al. 1993). In this study we leave B as a random variable, considering the possibility that B might represent other feedbacks in the system such as in albedo effects involving cloud and cryosphere or that B might change over time in the real climate system and so the sensitivity might really be a random variable taking on different values at different times.

3.3. PDFs of Climate Sensitivity

We produce likelihood-weighted PDFs of climate sensitivity by computing $O(10^6)$ annual-mean and annual-cycle model versions generated by perturbing the four key model-parameter settings (A, B, C, D). The PDFs exhibit very robust forms with longer "fat" tails as the tolerance variance is allowed to increase. They are close to Gaussian distributions as the tolerance gets smaller (Figure 27). This indicates that larger tolerance variances give rise to longer fat "tails" of the PDFs.

The upper panel of Figure 27 shows the PDF of sensitivity for the annual-mean-temperature results for three choices of the tolerance σ. The time dependent term in the annual-mean model drops out so that the parameter $C(\hat{r})$ vanishes. Note that the skewed

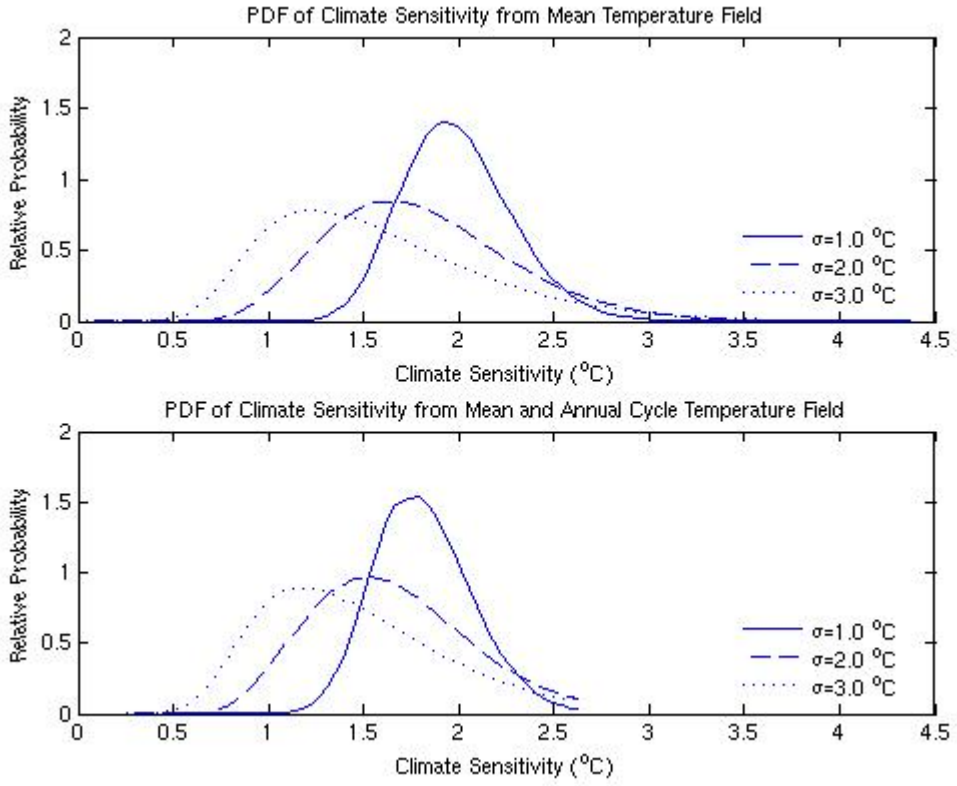

Fig. 27. Probability density function of climate sensitivity. These were obtained using a statistical estimate of modeled and observed surface temperature with different error tolerance variances σ. Upper panel based on O(10^6) model versions by perturbing three key parameters (B, D, A) of the annual-mean EBCM. Lower panel produced by calculating annual-cycle temperature through perturbing three key parameters (B, D, C) of the annual-cycle EBCM and then combining it with annual-mean temperature. A likelihood-weighted PDF of climate sensitivity by constraining the modeled temperature to the observations through the mean square error, is based on a measure of the goodness of fit for the modeled to the observed seasonal climate. Detailed in text.

PDFs which are relevant to large tolerances look similar to those in other published papers (e.g. Andronova and Schlesinger 2001; Forest et al. 2002; Gregory et al. 2002; Murphy et al. 2004; Stainforth et al. 2005), whereas as the tolerance gets smaller the PDF narrows and approaches a narrow gaussian shape. For $\sigma = 1^{\circ}\mathrm{C}$ the 5 to 95 % range for sensitivity is 1.53-2.49 ^{o}C, with a peak value of 1.92^{o}C and median 1.97 ^{o}C. This range is somewhat lower than the typical values reported in IPCC 2001. Note also that the value of B corresponding to this sensitivity is 2.27 W m^{-2} (deg C)$^{-1}$, which is very close to the value 2.26 W m^{-2} (^{o}C)$^{-1}$ estimated from satellite infrared data for clear skies and not far from the value 1.90 W m^{-2} (^{o}C)$^{-1}$ estimated for total sky (Graves et al. 1993). These satellite estimates were based upon mid-latitude correlations between surface temperature and broadband OLR observations.

The lower panel in Figure 27 shows the result when the annual-cycle temperature is combined with the annual-mean temperature. We can see that the dominant features of the PDFs are controlled by the annual-mean field. The characteristic indices such as peaks, median, 5-95% ranges of the sensitivity are very close to those in the upper panel.It indicates that the annual-mean surface temperature is much more sensitive to the atmospheric greenhouse-gas concentration level than the annual-cycle temperature. Like the upper panel above, larger values of tolerance lead to highly skewed distributions. This simple underlying property seems to explain much of the skewness found in other studies.

3.4. Uncertainty Analysis in Climate Sensitivity

We analyzed the squared error for some of the fits in order to check out the reason why models can differ so much in their sensitivities.

We first found that the function ε^2 is bowl shaped and concave upwards so that a minimum exists. This means that there is unique optimal choice for the parameters.

The optimal quantitative estimates of the model parameters were obtained by exploring the minimum range of the squared errors (Figure 28). The errors in annual-mean temperature show an ellipsoidal minimum range centered at coefficients B=2.17 W m^{-2} K^{-1}, D=2.2 W K^{-1}, A=170 W m^{-2}, which implies a multi-dimensional optimal range of the parameters for which the error in fitting the data is less than some value. If this value is small, the fit will be very good.

Figure 29 shows points in the (B, D) plane for which the value of the function $\varepsilon^2(A, B, D)$ lies between its minimum and 0.5 $(^oC)^2$ above the minimum. The circled asterisk symbol indicates the (B, D) location of the true minimum (B=2.17 W m^{-2} K^{-1},

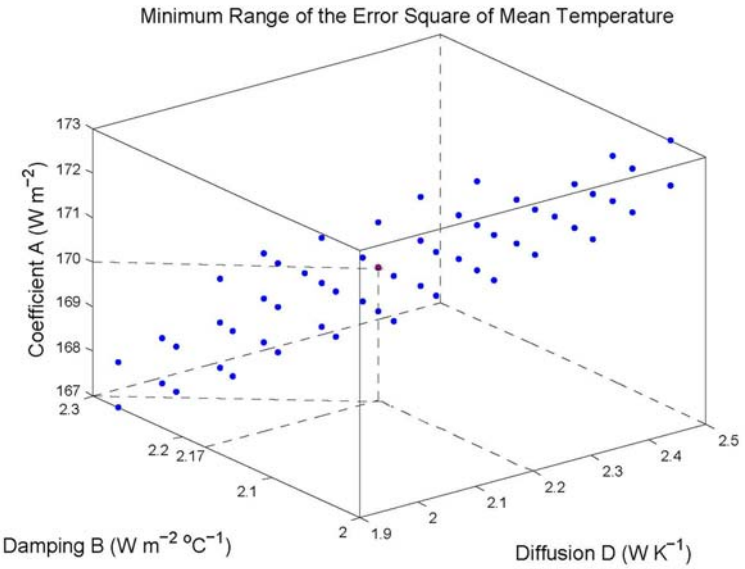

Fig. 28. Ellipsoidal minimum range of error square from modeled and observed annual-mean temperature. The error squares of these points are less than (the absolute minimum+0.2) (^{o}C)^{2}. The centered red star (*) is the true minimum position at B=2.17 W m^{-2} K^{-1}, D=2.2 W K^{-1}, A=170 W m^{-2}. Here a factor of earth radius squared has been absorbed into D.

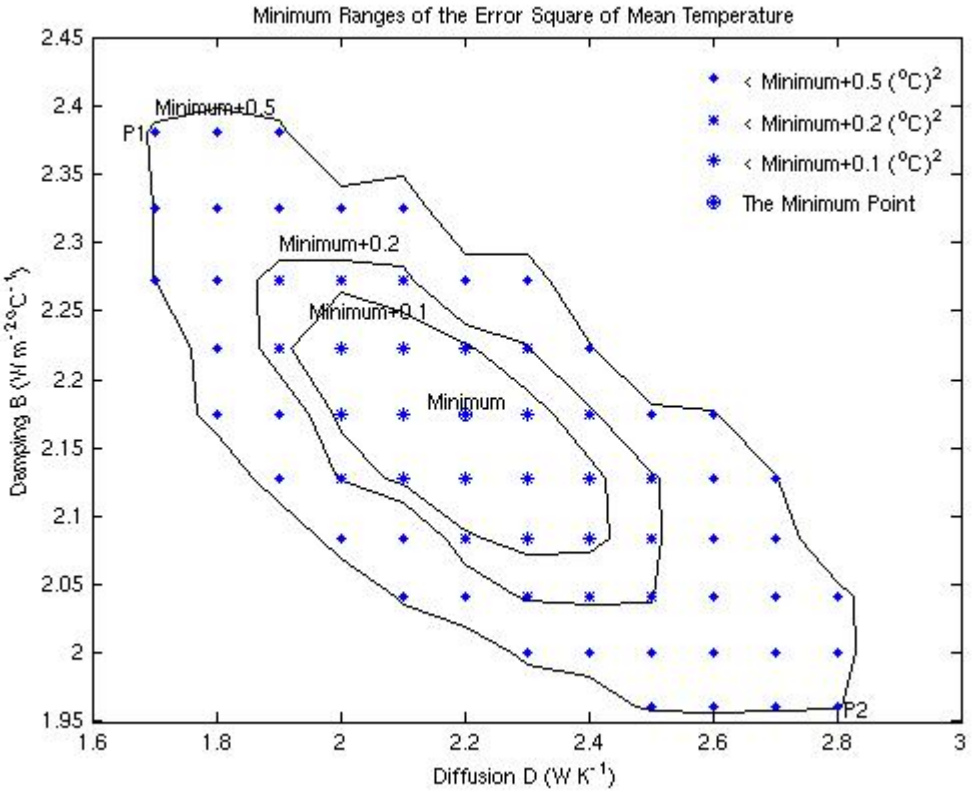

Fig. 29. Points projected in the B-D plane for which the mean square error falls below a certain level (0.5, 0.2, and 0.1 $(^oC)^2$ above the absolute minimum). The absolute minimum is for values B=2.17 W m^{-2} K^{-1}, D=2.2 W K^{-1}, A=170 W m^{-2}. The same quality of fit to the observation is shown to bring in a broad range of choices of B and D. The two extremes P1 and P2 have the same qulity of fit (mean square errors < 0.5 $(^oC)^2$ above the absolute minimum) but the change in their sensitivity is more than 20%. As in Fig. 28 a factor of earth radius squared has been absorbed into D.

D=2.2 W K^{-1}, A=170 W m^{-2}). It is interesting that for a large range of B ($B_{P1} = 2.38$ W $m^{-2}\,K^{-1}$, $B_{P2} = 1.96$ W $m^{-2}\,K^{-1}$) the values of the error squared in fitting are very close to the minimum value (only 0.5 $(^oC)^2$ above the minimum) (see points P_1 and P_2 in Figure 29). The rather broad and flat minimum in the mean square error indicates that models may obtain a wide range of sensitivity with relatively small penalty in fitting to observations.

Note that the same quality of fit to the data obtains ($\Delta\varepsilon^2 < 0.5$ $(^0C)^2$) for a broad range of choices of B and D. For the two extremes P1 and P2 in Figure 29, the change in sensitivity over this range is more than 20%.

Figure 30 shows the zonally averaged annual-mean temperatures for the data (solid line), for choice P1 (dashed line) and P2 (dotted line). There is very little difference in the dashed and dotted curves; in fact, they are closer to each other than to the solid curve representing the data. The poor fit of this model to the data in the Northern Hemisphere is due largely to the simplistic treatment of heat transport in the Tropics (Hadley Cell) in the EBCM.

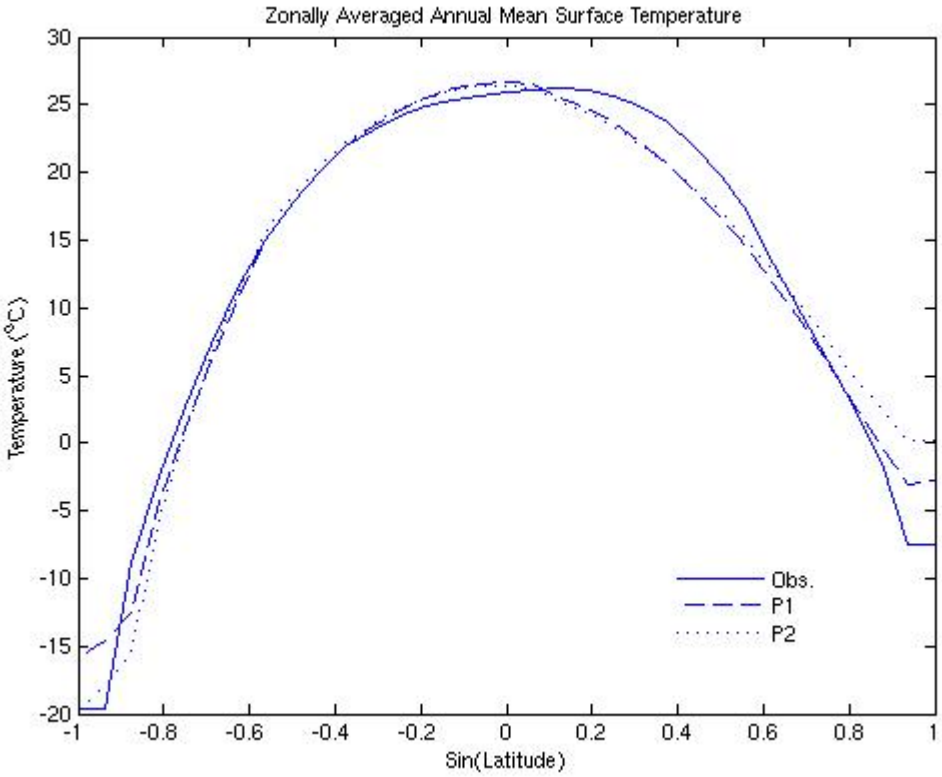

Fig. 30. Zonally averaged annual-mean temperature versus sine of latitude. Observational data (solid line), model for parameters from P1 of Figure 29 (dashed line), and model for parameters from P2 (dotted line). While neither model solution is a particularly good fit to the data, the two are very close to one another emphasizing that the mean square error is very insensitive to the choice along the diagonal of points in Figure 29.

It is significant that the results by optimizing model parameters are much better than those by intuitive guess (shown in Figures 31 and 32).

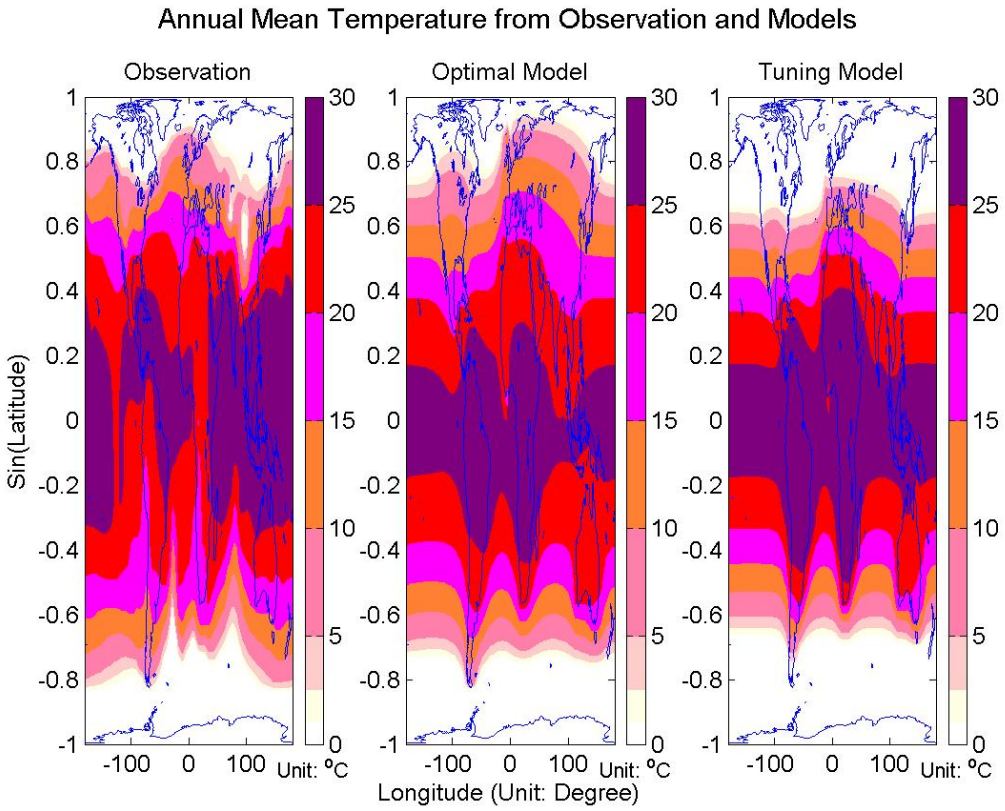

Fig. 31. Comparison of global annual-mean temperature from observation and model with different parameters. The left pattern is from observed data (Jones dataset). The middle one is model result by using optimal model parameters (B, D, A). The right one is model result by intuitively tuning model parameters (B, D, A) as in Table 1.

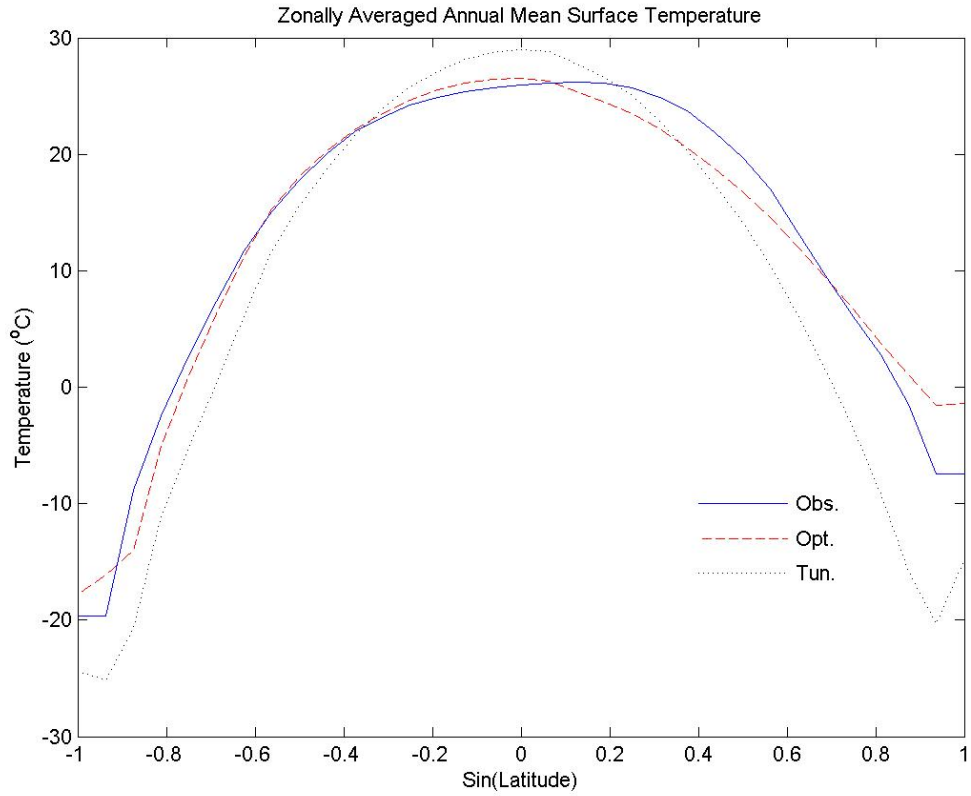

Fig. 32. Comparison of zonally averaged annual-mean temperature from observation and model with different parameters. The blue solid curve is from observed data (Jones dataset). The red dashed curve is model result by using optimal model parameters (B, D, A). The black dotted curve is model result by intuitively tuning model parameters (B, D, A) as in Table 1.

3.5. Summary

We investigated climate sensitivity by constraining the mean square errors of model results to the present climate, using multiple parameter perturbations – a linear statistical prediction scheme (Murphy et al. 2004), based on a family of simple climate

models (North et al. 1983) with only four key physical characteristic model parameters of atmospheric and surface processes. We found that a broad range of parameter settings in a model may lead to nearly the same mean square errors while the corresponding sensitivities can be far different from one another. These results provide us with some of the reasons why the ranges of the sensitivity from different GCM experiments can be so different. The PDFs with different levels of the error tolerance variance also explain the possible origin of the right-skewness pattern of the sensitivity found in many previous studies. Our approach to estimate the PDF of sensitivity is a useful tool for understanding the inter-model variability in climate models. The estimated PDF yields a 5-95% probability range of 1.53-2.49 ^{o}C for $\sigma = 1^{\circ}$C. The constraining method through mean square errors proves useful in optimal estimation of model parameters. It produces the optimal damping coefficient of 2.17 W m^{-2} (^{o}C)$^{-1}$, which is in good agreement with the estimated values from satellite infrared data (Graves et al.1993).

CHAPTER IV

CONCLUSIONS

The complete set of nonorthogonal Thermal Decay Modes generated through the medium of Energy Balance Climate Models (North et al. 1983) is a group of spatial physical modes having exponential decay characteristics. Their unique geographic patterns provide us with a clear visual impression on the relationship of the ocean and land modes. The nearly constant values of modal decay time scales over land and over ocean indicate that the spectral behaviors of ocean modes and land modes are close to white over a large range of spatial index. The dissipation time scales, which are ~2-3 months for ocean modes and about a few days for land modes, provide an important test for surface temperature studies. In contrast to previous studies with EBCMs we reduced the length scale over the ocean in order to match the spectrum in Figure 18. There is some theoretical justification based on the difference for large-scale ocean and atmosphere circulation (ocean Rossby Radius ~ 100km, compared to atmospheric ~ 1000km) and the importance of the vertical mixing to the ocean surface temperature. Testing the length scale over the ocean in models and data could be a subject of future research. The mode applications are successful in reproducing the global seasonal-cycle of surface temperature field and in testing the second moment statistics of the surface temperature fields. This implies that these thermal decay modes may be a useful reflection of the real world and thus could have further applications in climate studies.

The autocorrelation time scales of the mode amplitudes produced by data projection are similiar to the theoretical mode decay time scales. This is a kind of verification for the existence of the modes and their energy dissipation time scales. We can expand our surface temperature onto the modal patterns separating land and ocean surface temperature fields geographically, leading to applications for regional and global surface temperature studies. Output surface temperature data from complex ocean-atmosphere coupled models such as GCMs can be used to examine the autocorrelation time scales of the mode amplitudes by data projection and could be the subject of interest for future research on model intercomparison and testing the energy-dissipation time scales of surface temperature.

A second project provided an objective means of deriving the probability density function (PDF) of climate sensitivity to a doubling of atmospheric CO_2 concentration through the same family of energy balance climate models (North et al. 1983). The principal idea involves perturbing the four key model parameters (Murphy et al. 2004), then calculating $O(10^6)$ model realizations, then finally employing a prior distribution that constrains the PDF to favor better fits to the present climate. The origin of the spread of the sensitivity is demonstrated having something to do with the "tolerance" variance when constraining to better fits to the present climate. For a tight fit $\sigma = 1^{o}\mathrm{C}$, our procedure suggests 5-95% range of uncertainty in climate sensivity is 1.53-2.49 ^{o}C with a median of 1.97 ^{o}C. Looser fits lead to skewed distributions with lower typical values of sensitivity. The skewness of the PDF of the sensitivity is shown to be a fundamental property in EBCMs and related to the damping coefficient B, which is

inversely proportional to sensitivity. The constraining method through mean squared error calculation is an effective tool to estimate optimal values for model parameters and their spread. It may broadly be applied in different modeling studies although computational time is a serious problem in larger models. The uncertainty of climate sensitivity is shown to be difficult to eliminate because the same good fits may lead to a wide range of the sensitivity. Our findings are valid if climate models are tuned to fit observations of surface temperature alone. However, if models can in addition be tuned to produce accurate distributions of temperature above the surface, precipitation, sea ice, seasonal cycles of clouds at each height level, etc., the uncertainty of climate sensitivity may shrink. Extending our work to fit the last 100 years of surface temperatures is also of interest. Similarly constraining the fits of measures of errors in variance or covariance of the model (noise forced) versus the data is another valuable area of future researches.

REFERENCES

Allen, M. R. and W. J. Ingram 2002: Constrains on future changes in climate and hydrological cycle. *Nature*, **419**, 224-232.

Anderson, E., Z. Bai, C. Bischof, S. Blackford, J. Demmel, J. Dongarra, J. Du Croz, A. Greenbaum, S. Hammarling, A. McKenney and D. Sorensen, 2000: *LAPACK User' Guide*. 3rd ed., SIAM, 407 pp.

Andronova, N. G. and M. E. Schlesinger, 2001: Objective estimation of the probability density function for climate sensitivity. *J. Geophys. Res.*, **106**, 22605-22612.

Arrhenius, S., 1896: On the influence of carbonic acid on the air temperature of the ground. *Philos. Mag.*, **S5(41)**, 237-276.

Bell, T. L., 1980: Climate sensitivity from fluctuation dissipation: some simple model tests. *J. Atmos. Sci.*, **37**, 1700-1707.

Cahalan, R. F. and G. R. North, 1979: A stability theorem for energy-balance climate models. *J. Atmos. Sci.*, **36**, 1205-1216.

Chang, P., L. Ji and H. Li, 1997: A decadal climate variation in the tropical Atlantic Ocean from thermodynamic air-sea interactions, *Nature*, **385**, 516-518.

Crowley, T. J. and G. R. North, 1991: *Paleoclimatology*. Oxford University, 340 pp.

— and —, 1990: Modeling onset of glaciation. *Annals of Glaciol.*, **14**, 39-42.

— and —, l988: Abrupt climate change and extinction events in Earth history. *Science*, ***240***, 996-1002.

—, D. A. Short, J. G. Mengel and G. R. North, 1986: Role of seasonality in the evolution of climate during the last 100 million years. *Science*, **231**, 579-584.

Dines, W.H., 1917: The heat balance of the atmosphere. *J. Royal Meteorological Society*, **43**, 151-58.

Faulkner, F. D., 1976: *The Numerical Solution of the Helmholtz Equation on a Sphere*. NPS-53Fa76025, Naval Postgraduate School, Monterey, Calif, 20 pp.

Forest C. E., P. H. Stone, A. P. Sokolov, M. R. Allen, M. D. Webster, 2002: Quantifying uncertainties in climate system properties with the use of recent climate observations. *Science*, **295**, 113-117.

Frame D. J., B. B. B. Booth, J. A. Kettleborough, D. A. Stainforth, J. M. Gregory, M. Collins and M. R. Allen, 2005: Constraining climate forecasts: The role of prior assumptions. *Geophys. Res. Lett.*, **32**, L09702, doi: 10.1029/2004GL022241.

Gill, A. E., 1982: *Atmosphere-Ocean Dynamics*. Academic Press, 662 pp.

Goody, R., J. Anderson and G. R. North, 1998: Testing climate models: an approach, *Bull. Am. Met. Soc.*, **79**, 112541-112549.

Graves, C. E., W.-H. Lee and G. R. North, 1993: New parameterizations and sensitivities for simple climate models. *J. Geophys. Res.*, **98**, 5025-5036.

Gregory, J. M., R. Stouffer, S. Raper, N. Rayner and P. A. Stott, 2002: An observationally-based estimate of the climate sensitivity. *J. Clim.*, **15**, 3117-3121.

Haltiner, G. J. and R. T. Williams, 1980: *Numerical Prediction and Dynamic Meteorology*. John Wiley & Sons, 477 pp.

Hansen J., and S. Lebedeff, 1987: Global trends of measured surface air temperature. *J. Geophys. Res.*, **92**, 13345-13372.

—, L. Nazarenko, R. Ruedy, M. Sato, J. Willis et al., 2005: Earth's energy imbalance: confirmation and implications. *Science*, **308**, 1431-1435.

—, G. Russell, A. Lacis, I. Fung and D. Rind, 1985: Climate response times: Dependence on climate sensitivity and ocean mixing, *Science*, **229**, 857-859.

Harvey L. D. D., 2000: *Climate and Global Environmental Change*. Pearson Education, 240 pp.

Hasselmann, K., 1976: Stochastic climate models. Part I: Theory. *Tellus*, **28**, 473-484.

Horn, R. A. and C. R. Johnson, 1985: *Matrix Analysis*. Cambridge University press, 561 pp.

Huang, J., K. P. Bowman, 1992: The small ice cap instability in seasonal energy balance models. *Climate Dynamics*, **7**, 205-215.

Hunt, Garry E., R. Kandel and A. T. Mecherikunnel, 1986: A history of presatellite investigations of the Earth's radiation budget." *Rev. Geophys.*, **24**, 351-56.

Hyde, W. T., T. J. Crowley, K.-Y. Kim and G. R. North, 1989: A comparison of GCM and energy balance model simulations of seasonal temperature changes over the past 18,000 Years. *J. Climate*, **2**, 864-887.

—, K.-Y. Kim, T. J. Crowley and G. R. North, 1990: On the relation between polar continentality and climate: studies with a nonlinear seasonal energy balance model. *J. Geophys. Res.*, **95**, 18653-18668.

IPCC, 2001: *Climate Change: The Scientific Basis*, Cambridge Univ. Press, 881 pp.

—, 1990: *Climate Change: The IPCC Scientific Assessment*, Cambridge Univ. Press, 365 pp.

James, P. B. and G. R. North, 1982: The seasonal CO_2 cycle on Mars: an application of an energy balance climate model. *J. Geophys. Res.*, **87**, 10271-10283.

Kim, K.-Y. and G. R. North, 1995: Regional simulations of greenhouse warming including natural variability. *Bull. Am. Meteorol. Soc.*, **76**, 2171-2178.

— and —, 1993: EOF analysis of surface temperature field in a stochastic climate model. *J. Climate*, **6**, 1681-1690.

— and —, 1992: Seasonal cycle and second-moment statistics of a simple coupled climate system. *J. Geophys. Res.*, **97**, 20437-20448.

— and —, 1991: Surface temperature fluctuations in a stochastic climate model. *J. Geophys. Res.*, **96**, 18573-18580.

Kim, K.-Y., G. R. North and J.-P. Huang, 1996: EOF's of one-dimensional cyclostationary time series: computations, examples, and stochastic modeling. *J. Atmos. Sci.*, **53**, 1007-1017.

—, — and J. Huang, 1992: On the transient response of a simple coupled climate system. *J. Geophys. Res.*, **97**, 10069-10081.

Knutti, R., T. E. Stocker, F. Joos and G. K. Plattner, 2002: Constraints on radiative forcing and future climate change from observations and climate model ensembles. *Nature*, **416**, 719-723.

Lee, Wan-Ho and G. R. North, 1995: Small icecap instability in the presence of fluctuations. *Climate Dynamics*, **11**, 242-246.

Leith, C. E., 1975: Climate response and fluctuation dissipation. *J. Atmos. Sci.*, **32**, 2022-2026.

Leung, L.-Y. and G. R. North, 1991: Atmospheric variability on a zonally symmetric land planet. *J. Climate*, **4**, 753-765.

— and —, 1990: Information theory and climate prediction. *J. Climate*, **3**, 5-14.

Lin, R.-Q. and G. R. North, 1990: A study of abrupt climate change in a simple non-linear climate model. *Climate Dynamics*, **4**, 253-262.

McGuffie, K. and A. Henderson-Sellers, 1997: *A Climate Modelling Primer*. John Wiley & Sons, 253 pp.

Meehl, G. A., W. M. Washington, W. D. Collins, J. M. Arblaster, A. Hu, et al., 2005: How much more global warming and sea level rise?. *Science*, **307**, 1769-1772.

Mengel, J. G., D. A. Short and G. R. North, 1988: Seasonal snowline instability in an energy balance model. *Climate Dynamics*, **2**, 127-131.

Murphy, J. M., D. M. H. Sexton, D. N. Barnett, G. S. Jones, M. J. Webb, M. Collin and D. A. Stainforth, 2004: Quantification of modeling uncertainties in a large ensemble of climate change simulations. *Nature*, **430**, 768-772.

Newton, H. J., G. R. North and T. J. Crowley, 1990: Forecasting global ice volume. *J. Time Series Anal.*, **12**, 255-256.

North, G. R., 1990: Multiple solutions in energy balance climate models. *Global and Planetary Change*, **82**, 225-235.

—, 1984(a): Empirical orthogonal functions and normal modes. *J. Atmos. Sci.*, **41**, 879-886.

—, 1984(b): The small ice cap instability in diffusive climate models. *J. Atmos. Sci.*, **41**, 3390-3395.

—, 1975 (a): Theory of energy balance climate models. *J. Atmos. Sci.*, **32**, 2033-2043.

—, 1975 (b): Analytical solution to a simple climate model with diffusive heat transport. *J. Atmos. Sci.*, **32**, 1301-1307.

— and R. F. Cahalan, 1981: Predictability in a solvable stochastic climate model. *J. Atmos. Sci.*, **38**, 504-513.

— and J. A. Coakley, 1979: Differences between seasonal and mean annual energy balance model calculations of climate and climate change. *J. Atmos. Sci.*, **36**, 1189-1204.

— and J. A. Coakley, 1978: Simple seasonal climate models. *Meteorol. & Hydrol.*, **5**, 26-32.

— and T. J. Crowley, 1985: Application of a seasonal climate model to Cenozoic glaciation. *J. Geolog. Soc. (London)*, **142**, 475-482.

— and K.-Y. Kim, 1995: Detection of forced climate signals part II: simulation results. *J. Climate*, **8**, 409-417.

— and M. J. Stevens, 1998: Detecting climate signals in the surface temperature field. *J. Climate*, **11**, 563-577.

— and Q. Wu, 2001: Detecting climate signals using space-time EOFs. *J. Climate*, **14**, 1839-1862.

—, R. E. Bell and J. W. Hardin, 1993: Fluctuation dissipation in a general circulation model. *Climate Dynamics*, 8, 259-264.

—, R. F. Cahalan and J. A. Coakley, 1981: Energy balance climate models. *Rev. Geophys. Sp. Phys.*, **19**, 91-121.

— and J. G. Mengel and D. A. Short, 1983: A simple energy balance model resolving the seasons and the continents: application to the Milankovitch theory of the ice ages. *J. Geophys. Res.*, **88**, 6576-6586.

—, K.-Y. Kim, S. S. Shen and J. W. Hardin, 1995: Detection of forced climate signals part I: filter theory. *J. Climate*, **8**, 401-408.

Ramanathan, V. and J. A. Coakley, 1978: Climate modeling through radiative convective models. *Rev. Geophys. Space Phys.*, **16**, 465-489.

Salmun, H., R. F. Cahalan and G. R. North, 1980: Latitude-dependent sensitivity to stationary perturbations in simple climate models. *J. Atmos. Sci.*, **37**, 1874-1879.

Saltzman, B., 1978: A survey of statistical-dynamical models of the terrestrial climate. *Adv. Geophys.*, **20**, 183-303.

Schlesinger, M. E., 1989: Model projections of the climatic changes induced by increased atmospheric CO_2, in *Climate and Geosciences*, edited by A. Berger, S. H. Schneider and J.-C. Duplessy, Kluwer, pp. 375-415.

Schneider, S. H. and R. E. Dickinson, 1974: Climate modeling. *Rev.Geophys*, **12**, 447-493.

Shen, S.S. and G. R. North, 1999: A simple proof of the slope stability theorem for energy balance climate model. *Can. Appl. Math. Quarterly*, **7**, 201-215.

Short, D. A., J. G. Mengel, T. J. Crowley, W. T. Hyde and G. R. North, 1991: Filtering of Milankovitch cycles by Earth's geography. *Quaternary Res.*, **35**, 157-173.

—, G. R. North, T. D. Bess and G. L. Smith, 1984: Infrared parameterization and simple climate models. *J. Clim. & Appl. Meteorol.*, **23**, 1222-1233.

Stainforth D. A., T. Aina, C. Christensen, M. Collins, N. Faull, et al., 2005: Uncertainty in predictions of the climate response to rising levels of greenhouse gases. *Nature*, **433**, 403-406.

Stevens, M. J., 1997: Optimal estimation of the surface temperature response to natural and anthropogenic climate forcings over the past century. Ph.D. dissertation, Texas A&M University, 157 pp.

— and G. R. North, 1996: Detection of the climate response to the solar cycle. *J. Atmos. Sci.*, **53**, 2594-2608.

Stott, P. A. and J. A. Kettleborough, 2002: Origins and estimates of uncertainty in predictions of twenty-first century temperature rise. *Nature*, **416**, 723-726.

Sun, S. and J. E. Hansen, 2003: Climate simulations for 1951-2050 with a coupled atmosphere-ocean model. *J. Climate*, **16**, 2807-2826.

Von Storch J.-S., 2004: On statistical dissipation in GCM-climate. *Climate Dynamics*, **23**, 1-15.

Washington W. and Parkinson, C., 2005: *An Introduction to Three-Dimensional Climate Modeling*. University Science Books, 353 pp.

Wigley, T. M. L., C. M. Ammann, B. D. Santer and S. C. B. Raper, 2005: Effect of climate sensitivity on the response to volcanic forcing. *J. Geophys. Res.*, **110**, D09107, doi: 10.1029/2004JD005557.

APPENDIX A

PROPERTIES OF NON-ORTHOGONAL EIGENVALUES AND EIGENFUNCTIONS

A.1. The Eigenvalue Problem

The eigenvalue problem from equation (3) can be written as

$$H(\hat{r})\psi(\hat{r}) = \lambda C(\hat{r})\psi(\hat{r}) \tag{A1}$$

where the Hermitian operator (Horn and Johnson 1985) $H(\hat{r})$ is

$$H(\hat{r}) = -\nabla D(\hat{r}) \cdot \nabla + B)\psi(\hat{r}) \tag{A2}$$

The inner product is defined as

$$(a,b) = \sum_i a_i^* b_i \tag{A3}$$

where the * means Hermitian conjugate. It can be seen that

$$(a,b) = (b,a)^* \tag{A4}$$

The Hermitian conjugate of a matrix is defined as

$$M_{i,j}^+ = M_{j,i}^* \tag{A5}$$

where the $^+$ means Hermitian conjugate. So it has property of

$$(a, Mb) = (M^+ a, b) \tag{A6}$$

A.2. Reality of Eigenvalues

Take the inner product for (A1), we get

$$(\psi_m(\hat{r}), H(\hat{r})\psi_n(\hat{r})) = \lambda_n(\psi_m(\hat{r}), C(\hat{r})\psi_n(\hat{r})) \tag{A7}$$

Do the complex conjugate for (A7) and then apply (A4)

$$(H(\hat{r})\psi_n(\hat{r}), \psi_m(\hat{r})) = \lambda_n^*(C(\hat{r})\psi_n(\hat{r}), \psi_m(\hat{r})) \tag{A8}$$

Since $H(\hat{r})$ and $C(\hat{r})$ are Hermitian, we use (A6) to have

$$(\psi_n(\hat{r}), H(\hat{r})\psi_m(\hat{r})) = \lambda_n^*(\psi_n(\hat{r}), C(\hat{r})\psi_m(\hat{r})) \tag{A9}$$

Take the inner product for (A1), we can also get

$$(\psi_n(\hat{r}), H(\hat{r})\psi_m(\hat{r})) = \lambda_m(\psi_n(\hat{r}), C(\hat{r})\psi_m(\hat{r})) \tag{A10}$$

Compare (A9) with (A10)

$$\lambda_n^* = \lambda_m \tag{A11}$$

In particular, let m=n in (A11) to get

$$\lambda_n^* = \lambda_n \tag{A12}$$

That means the eigenvalues of problem (A1) are real.

A.3. Skewed Orthogonality of Eigenfunctions

To subtract (A9) from (A10) by using the property of reality of eigenvalues, we obtain

$$(\lambda_m - \lambda_n)(\psi_n(\hat{r}), C(\hat{r})\psi_m(\hat{r})) = 0 \tag{A13}$$

Then we have

$$(\psi_n(\hat{r}), C(\hat{r})\psi_m(\hat{r})) = \delta_{n,m} \tag{A14}$$

APPENDIX B

NUMERICAL FRAMEWORKS

B.1. Calculating Thermal Decay Modes

As we introduced in section 2.2, the Energy Balance Climate Model can be written as

$$C(\hat{r})\frac{\partial T(\hat{r},t)}{\partial t} - \nabla \cdot (D(\hat{r})\nabla T(\hat{r},t)) + A + BT(\hat{r},t) = F(\hat{r},t) \tag{B.1}$$

Its temperature departure is then written as

$$C(\hat{r})\frac{\partial \widetilde{T}(\hat{r},t)}{\partial t} - \nabla \cdot (D(\hat{r})\nabla \widetilde{T}(\hat{r},t)) + B\widetilde{T}(\hat{r},t) = \widetilde{F}(\hat{r},t) \tag{B.2}$$

If $\widetilde{F}(\hat{r},t)$ is assumed to be zero, we get a linear eigen problem (B.3) by setting $\widetilde{T}(\hat{r},t) = \psi(\hat{r})e^{-\lambda t}$.

$$(-\nabla D(\hat{r}) \cdot \nabla + B)\psi(\hat{r}) = \lambda C(\hat{r})\psi(\hat{r}) \tag{B.3}$$

We set longitude-sin(latitude) coordinate system for the sphere. Then (B.3) can be written as

$$-\lambda C(\varphi, y)\psi(\varphi, y) - \frac{\partial}{\partial y}[(1-y^2)(\frac{D}{r^2})\frac{\partial \psi(\varphi, y)}{\partial y}] - \frac{1}{(1-y^2)}\frac{\partial}{\partial \varphi}[(\frac{D}{r^2})\frac{\partial \psi(\varphi, y)}{\partial \varphi}]$$

$$+ B\psi(\varphi, y) = 0 \tag{B.4}$$

Where φ is longitude, y is sin(latitude), r is the radius of the Earth.

Then we set 64 (longitude) × 33 (sin(latitude)) grid points for our sphere. The differential equation of (B.4) can be written as follows. The technique of writing differential equations for climate models can be found in Haltiner and Williams (1980) and Faulkner (1976).

(1) At (i, j), where i=1, 2, …, M; j=2, 3, …, $N-1$

$$\psi_{i,j}[-\lambda C_{i,j} + B_{i.j} + \frac{\tilde{D}_{i,j+\frac{1}{2}}}{\Delta y^2}(1-y^2_{j+\frac{1}{2}}) + \frac{\tilde{D}_{i,j-\frac{1}{2}}}{\Delta y^2}(1-y^2_{j-\frac{1}{2}})] + \frac{\tilde{D}_{i+\frac{1}{2},j} + \tilde{D}_{i-\frac{1}{2},j}}{(1-y_j^2)\Delta\varphi^2}]$$

$$+\psi_{i-1,j}[\frac{-\tilde{D}_{i-\frac{1}{2},j}}{(1-y_j^2)\Delta\varphi^2}] + \psi_{i+1,j}[\frac{-\tilde{D}_{i+\frac{1}{2},j}}{(1-y_j^2)\Delta\varphi^2}]$$

$$+\psi_{i,j-1}[\frac{-\tilde{D}_{i,j-\frac{1}{2}}(1-y^2_{j-\frac{1}{2}})}{\Delta y^2}] + \psi_{i,j+1}[\frac{-\tilde{D}_{i,j+\frac{1}{2}}(1-y^2_{j+\frac{1}{2}})}{\Delta y^2}] = 0 \qquad \text{(B.5)}$$

Where $\tilde{D} = \frac{D}{r^2}$, M=33, N=64.

(2) At the South Pole (j=1),

$$\psi_1[-\lambda C_1 + B_1 + \frac{4(1-y^2_{1+\frac{1}{2}})}{M\Delta y^2}\sum_{i=1}^{M}\tilde{D}_{i,1+\frac{1}{2}}] - \frac{4(1-y^2_{1+\frac{1}{2}})}{M\Delta y^2}\sum_{i=1}^{M}\tilde{D}_{i,1+\frac{1}{2}}\psi_{i,2} = 0 \qquad \text{(B.6)}$$

(3) At the North Pole (j=N), similiarly we get

$$\psi_N[-\lambda C_N + B_N + \frac{4(1-y^2_{N-\frac{1}{2}})}{M\Delta y^2}\sum_{i=1}^{M}\tilde{D}_{i,N-\frac{1}{2}}] - \frac{4(1-y^2_{N-\frac{1}{2}})}{M\Delta y^2}\sum_{i=1}^{M}\tilde{D}_{i,N-\frac{1}{2}}\psi_{i,N-1} = 0 \qquad \text{(B.7)}$$

Now we can combine (B.5), (B.6) and (B.7) to get a matrix equation

$$[-\lambda\tilde{C}_{K,K} + \tilde{H}_{K,K}]\tilde{\psi}_{K,1} = 0$$

From the matrix equation, we have linear eigen problem

$$\tilde{C}_{K,K}^{-1}\tilde{H}_{K,K}\tilde{\psi}_{K,1} = \lambda\tilde{\psi}_{K,1} \tag{B.8}$$

where $\tilde{C}_{K,K}$ is $K \times K$ diagonal matrix , $\tilde{H}_{K,K}$ is $K \times K$ Hermitian matrix.

(B.8) can be directly solved by using LAPACK (Anderson et al. 2000), a free Fortran library available at *www.netlib.org*.

B.2. Calculating Seasonal Forcing Responses

By (B.2), the temperature responses to periodic forcings can be written as

$$C(\varphi, y)\frac{\partial T(\varphi, y, t)}{\partial t} - \frac{\partial}{\partial y}[(1-y^2)\tilde{D}\frac{\partial T(\varphi, y, t)}{\partial y}] - \frac{1}{(1-y^2)}\frac{\partial}{\partial \varphi}[\tilde{D}\frac{\partial T(\varphi, y, t)}{\partial \varphi}]$$

$$+ BT(\varphi, y, t) = F_{\omega}(\varphi, y, t)e^{-i\omega t} \tag{B.9}$$

Where φ is longitude, y is sin(latitude), $\tilde{D} = \frac{D}{r^2}$, r is the radius of the Earth. The temperature $T(\varphi, y, t)$ can be written as (detailed in 2.4)

$$T(\varphi, y, t) = \sum_n a_n(t)\psi_n(\varphi, y) \tag{B.10}$$

with

$$a_n(t) = a_{\omega,n}e^{-i\omega t} \tag{B.11}$$

$$a_{\omega,n} = \frac{(\psi_{n,} F_{\omega})}{\lambda_n - i\omega} \tag{B.12}$$

By plugging (B.12) into (B.11) and then putting the $a_n(t)$ expression back into (B.10), we get

$$T(\varphi, y, t) = \left|A(\varphi, y)\right| e^{i\alpha(\varphi, y)} e^{-i\omega t} \tag{B.13}$$

with

$$\left|A(\varphi, y)\right| = (a^2 + b^2)^{1/2} \tag{B.14}$$

$$\alpha(\varphi, y) = arctg(b/a) \tag{B.15}$$

$$a = \sum_{n=1}^{m} \frac{(\psi_n, F_\omega)}{\lambda_n^2 + \omega^2} \lambda_n \psi_n(\varphi, y) \tag{B.16}$$

$$b = \sum_{n=1}^{m} \frac{(\psi_n, F_\omega)}{\lambda_n^2 + \omega^2} \omega \psi_n(\varphi, y) \tag{B.17}$$

where $\left|A(\varphi, y)\right|$ and $\alpha(\varphi, y)$ are the amplitude and lag of the temperature response to the periodic forcing, respectively.

Therefore, we use the eigenvalues λ_n and eigenfunctions $\psi_n(\varphi, y)$ which we got from section B.1 to calculate the amplitude $\left|A(\varphi, y)\right|$ and lag $\alpha(\varphi, y)$ of the temperature response to the periodic forcing $F_\omega(\varphi, y, t)e^{-i\omega t}$. Note that solar radiation forcing $F_\omega(\varphi, y, t)e^{-i\omega t}$ is known for annual and semi-annual cycles (see (2.17)-(2.19)).

B.3. Calculating Mean Forcing Response

If the temperature is assumed to be driven by annual-mean forcing $F(\hat{r})$, the temperature response to this forcing can be written as (see (2.16))

$$-\nabla \cdot (D(\hat{r})\nabla T(\hat{r})) + A + BT(\hat{r}) = F(\hat{r}) \tag{B.18}$$

In our longitude-sin(latitude) coordinate system, (B.18) is written as

$$-\frac{\partial}{\partial y}[(1-y^2)(\tilde{D}(\varphi,y))\frac{\partial T(\varphi,y)}{\partial y}]+B(\varphi,y)T(\varphi,y)=A+F(y) \qquad \text{(B.19)}$$

Where φ is longitude, y is sin(latitude), $\tilde{D}=\frac{D}{r^2}$, r is the radius of the Earth.

The differential equation of (B.19) can be written as follows.

(1) At (i , j), where i =1, 2, …, M ; j =2, 3, …, $N-1$

$$T_{i,j}[B_{i.j}+\frac{\tilde{D}_{i,j+\frac{1}{2}}}{\Delta y^2}(1-y^2_{j+\frac{1}{2}})+\frac{\tilde{D}_{i,j-\frac{1}{2}}}{\Delta y^2}(1-y^2_{j-\frac{1}{2}})]+\frac{\tilde{D}_{i+\frac{1}{2},j}+\tilde{D}_{i-\frac{1}{2},j}}{(1-y_j^2)\Delta\varphi^2}]$$

$$+T_{i-1,j}[\frac{-\tilde{D}_{i-\frac{1}{2},j}}{(1-y_j^2)\Delta\varphi^2}]+T_{i+1,j}[\frac{-\tilde{D}_{i+\frac{1}{2},j}}{(1-y_j^2)\Delta\varphi^2}]$$

$$+T_{i,j-1}[\frac{-\tilde{D}_{i,j-\frac{1}{2}}(1-y^2_{j-\frac{1}{2}})}{\Delta y^2}]+T_{i,j+1}[\frac{-\tilde{D}_{i,j+\frac{1}{2}}(1-y^2_{j+\frac{1}{2}})}{\Delta y^2}]=A+F_{i,j} \qquad \text{(B.20)}$$

(2) At the South Pole (j =1),

$$T_1[B_1+\frac{4(1-y^2_{1+\frac{1}{2}})}{M\Delta y^2}\sum_{i=1}^{M}\tilde{D}_{i,1+\frac{1}{2}}]-\frac{4(1-y^2_{1+\frac{1}{2}})}{M\Delta y^2}\sum_{i=1}^{M}\tilde{D}_{i,1+\frac{1}{2}}T_{i,2}=A+F_1 \qquad \text{(B.21)}$$

(3) At the North Pole (j =N), similiarly we get

$$T_N[B_N+\frac{4(1-y^2_{N-\frac{1}{2}})}{M\Delta y^2}\sum_{i=1}^{M}\tilde{D}_{i,N-\frac{1}{2}}]-\frac{4(1-y^2_{N-\frac{1}{2}})}{M\Delta y^2}\sum_{i=1}^{M}\tilde{D}_{i,N-\frac{1}{2}}T_{i,N-1}=A+F_N \qquad \text{(B.22)}$$

Combining (B.20), (B.21) and (B.22), we get

$$I_{K,K}T_{K,1}=F_{K,1} \qquad \text{(B.23)}$$

(B.23) is a linear problem and can be solved smoothly by using LAPACK. Note that the annual-mean solar radiation forcing $F(\varphi, y)$ is known from (2.17)-(2.19).

APPENDIX C

MODE'S AUTOCORRELATION TIME SCALE

For each-mode amplitude a_n forced by white-noise forcing, by (2.9) we have

$$\rho(\tau_n) = \frac{< a_n(t) a_n(t+\tau_n) >}{< a_n(t) a_n(t) >} = e^{-\lambda_n \tau_n} \tag{C.1}$$

Where $1/\lambda_n$ is the decay time scales of mode n, i.e., λ_n is the eigenvalue.

One derivation for (C.1) is given here.

By (2.8) we have

$$\dot{a}_n(t) + \lambda_n a_n(t) = (\psi_n(\hat{r}), WN(\hat{r})) = WN \tag{C.2}$$

where WN denotes white noise.

By plugging $WN = WN_\omega e^{i\omega t}$ and $a_n(t) = a_n^\omega e^{i\omega t}$ into (C.2), we get

$$i\omega a_n^\omega + \lambda_n a_n^\omega = WN_\omega \tag{C.3}$$

So,

$$\left| a_n^\omega \right|^2 = \frac{\left| WN_\omega \right|^2}{\omega^2 + \lambda_n^2} \tag{C.4}$$

The corresponding autocorrelation function is then

$$R(\tau_n) = F^{-1}(\left| a_n^\omega \right|^2) = F^{-1}(\frac{\left| WN_\omega \right|^2}{\omega^2 + \lambda_n^2}) = \frac{\left| WN_\omega \right|^2}{2\lambda_n} e^{-\lambda_n \tau_n} \tag{C.5}$$

Therefore, the normalized autocorrelation function is $\rho(\tau_n) = e^{-\lambda_n \tau_n}$ as in (C.1).

VITA

Wei Wu
Department of Atmospheric Sciences, 1204 Eller O&M Building, Texas A&M University, College Station, Texas 77843-3150

EDUCATION

Texas A&M University, College of Geosciences College Station, TX
Ph.D., Oceanography, December 2005

Ocean University of China Qingdao, China
M.S., Environmental Oceanography, July 1994

Ocean University of China Qingdao, China
B.S., Applied Mathematics, July 1988

PROFESSIONAL EXPERIENCES

Texas A&M University, U.S.A
Graduate Research Assistant, Oceanography Department. 2001 – 2005

Ocean University of China, Qingdao, China
Lecturer, Oceanography Department. 1994 – 2001

Flinders University of SA, Adelaide, Australia
Visiting Scholar, Earth Science, March-July 2000

Ocean University of China, Qingdao, China
Graduate Research Assistant, Oceanography Department. 1991 – 1994